$Ba_6(Cu_xZ_y)Sn_4S_{16}$(Z=Mg, Mn, Zn, Cd, In, Bi, Sn): High Chemical Flexibility Resulting in Good Nonlinear Optical Properties

Bingheng Ji [a], Kui Wu [b], Yunhua Chen [c, d], Fei Wang [e], Aaron J Rossini [c, d], Bingbing Zhang [b] *, Jian Wang [a] *

[a] Department of Chemistry and Biochemistry, Wichita State University, Wichita, Kansas 67260, United States

[b] College of Chemistry and Environmental Science, Hebei University, Key Laboratory of Analytical Science and Technology of Hebei Province, Baoding 071002, China

[c] U.S. DOE Ames Laboratory, Ames, IA 50011, United States

[d] Department of Chemistry, Iowa State University, Ames, Iowa, 50011, United States

[e] Department of Chemistry, Missouri State University, Springfield, Missouri, 65897, United States

Abstract

Seven acentric sulfides $Ba_6(Cu_xZ_y)Sn_4S_{16}$(Z=Mg, Mn, Zn, Cd, In, Bi, Sn) were grown by a high temperature salt flux method. The crystal structure of $Ba_6(Cu_xZ_y)Sn_4S_{16}$(Z=Mg, Mn, Zn, Cd, In, Bi, Sn) compounds were determined by single crystal X-ray diffraction with the aid of solid-state NMR spectroscopy. $Ba_6(Cu_xZ_y)Sn_4S_{16}$(Z=Mg, Mn, Zn, Cd, In, Bi) compounds are isostructural and crystallize in the $Ba_6Ag_4Sn_4S_{16}$ structure type. The Sn containing compound exhibits high structure similarity to $Ba_6(Cu_xZ_y)Sn_4S_{16}$(Z=Mg, Mn, Zn, Cd, In, Bi) with the presence of an interstitial atomic position partially occupied by Sn atoms. The chemical bonding characteristics of $Ba_6(Cu_{2.9}Sn_{0.4})Sn_4S_{16}$ were understood with electron localization function calculations coupled with crystal orbital Hamilton population calculations. The Ba-S interactions and Cu-S interactions are dominantly ionic, but the Sn-S interactions consist of strong covalent bonding characteristics

in $Ba_6(Cu_{2.9}Sn_{0.4})Sn_4S_{16}$. The monovalent Cu atoms, mixed with certain metals with various oxidation states, significantly shift the optical properties of $Ba_6(Cu_xZ_y)Sn_4S_{16}$(Z=Mg, Mn, Zn, Cd, In, Bi) compounds. This results in good balance between second harmonic generation (SHG) response and laser damage threshold (LDT). $Ba_6(Cu_{1.9}Zn_{1.1})Sn_4S_{16}$ possesses a high SHG response and a high LDT of 2.8 × AGS and 3× AGS respectively. A DFT calculation revealed that $[CuS_4]$ tetrahedra and $[SnS_4]$ tetrahedra significantly contribute to the second harmonic generation response in $Ba_6(Cu_2Mg)Sn_4S_{16}$, which also confirmed that $[CuS_4]$ tetrahedra are crucial for the stability and optical properties of the $Ba_6(Cu_xZ_y)Sn_4S_{16}$(Z=Mg, Mn, Zn, Cd, In, Bi, Sn) compounds revealed by electronic structure analysis.

Introduction

The second harmonic generation process is widely employed to extend the frequency range of lasers, which are crucial for scientific research and optoelectronic industry applications [1-4]. Nonlinear optical (NLO) materials are a key component for the second harmonic generation process [5-15]. A good NLO material should fulfill a series of criteria, including a suitable bandgap for good transmission at the required spectrum region, a large second-harmonic generation (SHG) coefficient for high energy conversion efficiency, a high laser damage threshold (LDT) for more intense and steady laser outputs, moderate birefringence for phase-matching capability, excellent stability such as thermal-, chemical- and air-stability, and the ability to grow large crystals [16-19]. Balancing these criteria is not easy since many of these parameters are intrinsically correlated [20-22]. For example, a material with large bandgap should generally have a high LDT but the SHG coefficients would be expected to be low. Inversely, small bandgap materials are more likely to

have large SHG coefficients but with the price of sacrificing LDT [9, 23, 24]. Designing novel NLO materials with a balance of all the required properties is the major focus of this field.

An NLO system, with great chemical flexibility, opens a window to balance all desired properties of NLO materials [25]. A few good examples are the diamond-like structure compounds (Li_2CdSnS_4 [26], α-Li_2ZnGeS_4 [27], Li_2MnSnS_4 [28], $Mg_2In_3Si_2P_7$ [29], $LiZn(OH)CO_3$ [30], α-Cu_2ZnSiS_4 [31], $HgCuPS_4$ [32], $Li_4HgSn_2Se_7$ [33], and $RE_6B_xC_yCh_{14}$ (RE=Y, La-Lu; B=Si, Ge, Sn, Al, Ga; C= monovalent M^+ (Ag, Na, Li, etc.), divalent M^{2+} (Mg, Cr, Ni, Zn, etc.), trivalent M^{3+} (Al, In, Ga, etc.), tetravalent M^{4+} (Si, Ge, Sn) and pentavalent M^{5+} (Sb); Ch=S, Se) which have demonstrated that an excellent balance of NLO properties originating from their chemical flexibility[34-41]. Recently, another system, $II_6I_4V_4Ch_{16}$(II=Sr, Ba; I=Li, Cu; Ag, IV=Ge, Sn; Ch=S, Se), has been heavily studied due to their emerging NLO properties and the demonstration of their excellent chemical flexibility [42-51]. In this work, we discovered another seven compounds belonging to the $II_6I_4V_4Ch_{16}$(II=Sr, Ba; I=Li, Cu, Ag; IV=Ge, Sn; Ch=S, Se) family. The chemical flexibility of the $II_6I_4V_4Ch_{16}$(II=Sr, Ba; I=Li, Cu, Ag; IV=Ge, Sn; Ch=S, Se) family is further expanded with the discovery of trivalent dopants for the first time. The synthesis, crystal growth, crystal structure, and linear and nonlinear optical properties of $Ba_6(Cu_xZ_y)Sn_4S_{16}$(Z=Mg, Mn, Zn, Cd, In, Bi, Sn) are discussed in this work. $Ba_6(Cu_xZ_y)Sn_4S_{16}$(Z=Mg, Mn, Zn, Cd, In, Bi, Sn) compounds possess a good balance between SHG and LDT due to their high chemical flexibility.

Experimental

Reagents

All reactants in this work were used as received without further processing: barium rod (Sigma Aldrich, 99+%), copper powder (Alfa Aesar, 99.5%), zinc granules (Alfa Aesar, 99.8%), magnesium turnings (Alfa Aesar, 99.8%), manganese pieces (Alfa Aesar, 99.9%), cadmium shot

(Alfa Aesar, 99.8%), indium shot (Alfa Aesar, 99.9%), bismuth pieces (Alfa Aesar, 99.99%), sulfur powder (Alfa Aesar, 99.5%), and potassium iodide (Sigma Aldrich, 99.5%). These reactants were stored in an Argon-filled glovebox which maintained moisture and oxygen levels below 0.3 ppm. All preparations were done in the glovebox or under vacuum.

Synthesis

The overall crystal growth process was aided by KI salt flux. For the compound $Ba_6(Cu_{2.9}Sn_{0.4})Sn_4S_{16}$, 0 .4 g total of the reactants were loaded in a molar ratio of Ba:Cu:Sn:S = 6:4:4:16 and mixed with 0.4g KI flux into a carbonized silica tube. For the compounds $Ba_6(Cu_xZ_y)Sn_4S_{16}$ (Z=Mg, Mn, Zn, Cd), the reactant elements were loaded at the molar ratio of Ba:Cu:Z:Sn:S=6:2:1:4:16 (Z = Mg, Mn, Zn, Cd) (0.4 g total) mixed with 0.4 g KI salt flux into carbonized silica ampules. For the compounds $Ba_6(Cu_xZ_y)Sn_4S_{16}$ (Z=In, Bi), the ratios of reactants were changed to Ba:Cu:Z:Sn:S=6:2.5:0.5:4:16 (Z = In, Bi). The 0.4 g element mixtures were mixed with 0.4 g KI and loaded into carbonized silica tubes. Then, the silica tubes were flamed-sealed under a vacuum of 10^{-2} Torr and heated within a programmable box furnace. All samples shared the same temperature profile. Samples were heated up to 800 °C in 10 hours, held for 48 hours at this temperature, and then slowly cooled to 650 °C within 100 h. Samples were kept for 10 h at 650 °C before the furnace was shut off. The KI flux was removed with DI water. All samples are stable in air and water with no obvious change found by powder X-ray diffraction. Within dry air, all samples are stable for several months. More divalent and trivalent metals including Ni^{2+}, Fe^{2+}, Ga^{3+} were tried to replace Cu, which were not successful.

UV-Vis Measurements

Diffuse-reflectance spectra were documented on a PERSEE-T8DCS UV-Vis spectrophotometer equipped with an integration sphere in the wavelength range of 230−850 nm at room temperature.

The reflectance data, R were recorded and converted to the Kubelka-Munk function, $f(R)=(1-R)^2(2R)^{-1}$. The Tauc plots, $(KM*E)^2$ and $(KM*E)^{1/2}$, were applied to estimate direct and indirect bandgap, respectively.

Single-crystal X-ray crystallography (SCXRD)

Data collections were performed at 298(2) K using a Bruker Kappa APEX II diffractometer with graphite monochromatic Mo-K_α radiation (wavelength =0.71073 Å). Data integration and reduction, together with global unit cell refinements, were performed in the APEX2 software [52]. The absorption correction method was the multi-scan method [52]. The structures were solved by direct methods and refined by full matrix least-squares methods on F^2 using the SHELX package with anisotropic displacement parameters for all atoms [53]. In the last refinement cycles, the atomic positions for all compounds were standardized using the program Structure TIDY [54,55] Details of the data collection and structure refinement are provided in **Table S1**. Atomic coordinates and selected distances are listed in **Tables S2 and S3**. The deviation of the occupancies of Wyckoff position *12a* in $Ba_6(Cu_xZ_y)Sn_4S_{16}$(Z=Mg, Mn, Zn, Cd, In, Bi) was refined and summarized in **Table S2**. During the structural model refinement process, the occupancy of the Cu atomic positions were released first, then Z atoms (Z= Mg, Mn, Zn, Cd, In, Bi) were added to the Cu position via the adding of restrictions of equaling atomic displacement parameters (ADP) and equaling atomic positions of Z atoms and Cu atoms with total occupancy of Z + Cu= 1. For the last refinement cycle, the occupancy of Sn atoms was refined as well. The occupancy of Sn atoms was no less than 98% for $Ba_6(Cu_xZ_y)Sn_4S_{16}$(Z=Mg, Mn, Zn, Cd, In, Bi) compounds. Hence, we conclude that the Sn atoms are fully occupied in $Ba_6(Cu_xZ_y)Sn_4S_{16}$(Z=Mg, Mn, Zn, Cd, In, Bi) compounds. The single crystal refinements determined the chemical formula of $Ba_6(Cu_xZ_y)Sn_4S_{16}$(Z= Sn, Mg, Mn, Zn, Cd, In, Bi) compounds as $Ba_6(Cu_{2.9(1)}Sn_{0.4(1)})Sn_4S_{16}$,

$Ba_6(Cu_{1.9(1)}Mg_{1.1(1)})Sn_4S_{16}$, $Ba_6(Cu_{2.2(1)}Mn_{0.8(1)})Sn_4S_{16}$, $Ba_6(Cu_{1.9(1)}Zn_{1.1(1)})Sn_4S_{16}$, $Ba_6(Cu_{2.5(1)}Cd_{0.5(1)})Sn_4S_{16}$, $Ba_6(Cu_{2.5(1)}In_{0.5(1)})Sn_4S_{16}$, and $Ba_6(Cu_{2.6(1)}Bi_{0.4(1)})Sn_4S_{16}$ for Z = Sn, Mg, Mn, Zn, Cd, In, and Bi, respectively. The chemical formulas determined by single crystal X-ray diffraction were verified by energy dispersive X-Ray analysis (EDX) measurements (**Table S4**). The EDX results verified the accuracy of single crystal X-ray results. To simplify the presentation of $Ba_6(Cu_xZ_y)Sn_4S_{16}$(Z=Mg, Mn, Zn, Cd, In, Bi, Sn) compounds, the standard deviations of occupancies of the Wyckoff position *12a,* and the interstitial Sn atomic positions, are excluded. Crystallographic data for $Ba_6(Cu_xZ_y)Sn_4S_{16}$(Z=Mg, Mn, Zn, Cd, In, Bi, Sn) compounds have been deposited to the Cambridge Crystallographic Data Centre, CCDC, 12 Union Road, Cambridge CB21EZ, UK. Copies of the data can be obtained free of charge by quoting the depository numbers CCDC - 2115184 ($Ba_6(Cu_{2.9}Sn_{0.4})Sn_4S_{16}$,), CCDC - 2115187 ($Ba_6(Cu_{1.9}Mg_{1.1})Sn_4S_{16}$), CCDC - 2115186 ($Ba_6(Cu_{2.2}Mn_{0.8})Sn_4S_{16}$), CCDC - 2115185 ($Ba_6(Cu_{1.9}Zn_{1.1})Sn_4S_{16}$), CCDC - 2115190 ($Ba_6(Cu_{2.5}Cd_{0.5})Sn_4S_{16}$), CCDC - 2115189 ($Ba_6(Cu_{2.5}In_{0.5})Sn_4S_{16}$), CCDC - 2115188 ($Ba_6(Cu_{2.6}Bi_{0.4})Sn_4S_{16}$).

Powder X-ray diffraction (PXRD) and EDX analysis

Powder X-ray diffraction data were collected at room temperature using a Rigaku Mini Flex II diffractometer with Cu-*K*α radiation (λ =1.5406 Å) in the range 2θ = 10° – 80°, at a scan step of 0.04° with ten seconds exposure time. All simulated PXRD patterns were calculated based on a structure model refined from single crystal diffraction. All samples are a single phase, as shown in **Figure 1** and **Figure S1**. EDX data were recorded at room temperature using a Phenom Pharos G2 Desktop FEG-SEM.

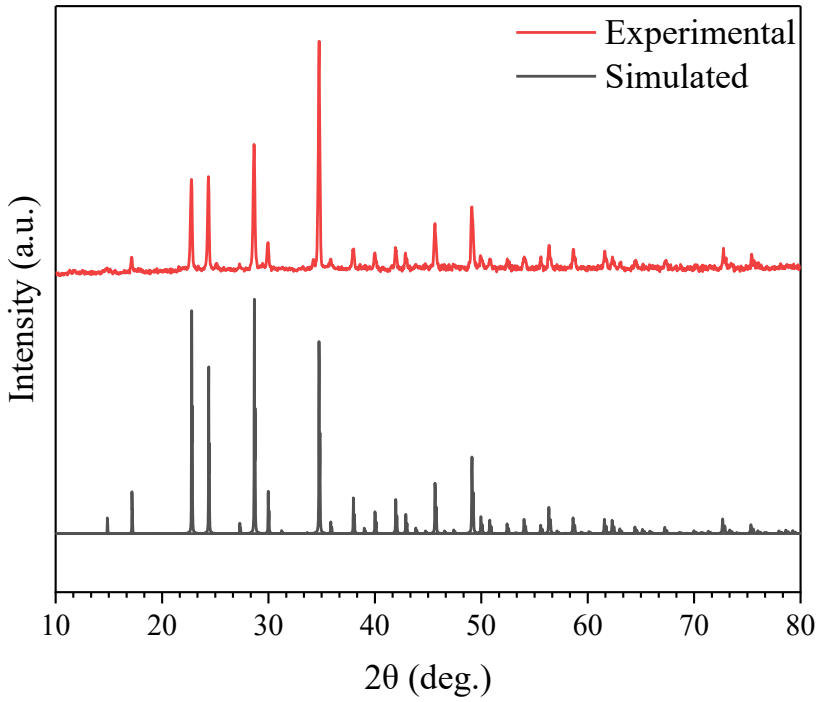

Figure 1. Experimental powder X-ray diffraction pattern for compound $Ba_6(Cu_{2.2}Mn_{0.8})Sn_4S_{16}$ and simulated PXRD data.

Second harmonic generation (SHG) measurements and LDT test

The SHG measurements of powder samples of $Ba_6(Cu_xZ_y)Sn_4S_{16}$(Z=Mg, Mn, Zn, Cd, In, Bi, Sn), sieved into five different particle sizes of 38.5-54, 54-88, 88-105, 105-150, 150-200 μm, were performed through the Kurtz and Perry method by a Q-switch laser (2.09 μm, 3 Hz, 50 ns) [56]. The homemade $AgGaS_2$ crystals served as reference, at the same particle sizes, for comparison with the seven compounds. The LDTs of $Ba_6(Cu_xZ_y)Sn_4S_{16}$(Z=Mg, Mn, Zn, Cd, In, Bi, Sn) compounds were evaluated on powder samples (150−200 μm) with a pulsed YAG laser (1.06 μm, 10 ns, 10 Hz). The judgment criterion is as follows: with increasing laser energy, the color change of the powder sample is constantly observed by an optical microscope to determine the damage threshold. To adjust different laser beams, an optical concave lens is added to the laser path. The damaged spot is measured by the scale of the optical microscope.

Electronic structure calculations

$Ba_6(Cu_{2.9}Sn_{0.4})Sn_4S_{16}$ and $Ba_6(Cu_{1.9}Mg_{1.1})Sn_4S_{16}$ were selected to study their electronic structures via density functional theory (DFT) calculations. For $Ba_6(Cu_{2.9}Sn_{0.4})Sn_4S_{16,}$ a model structure was built by removing the interstitial Sn atoms and setting the occupancy of Cu atoms to 100%, which resulted in a chemical formula of $Ba_6Cu_3Sn_4S_{16}$. To simulate the Cu/Mg site sharing in $Ba_6(Cu_{1.9}Mg_{1.1})Sn_4S_{16}$, we lowered the symmetry from the experimental $I\bar{4}3d$ to $I\bar{4}2d$, which splits the shared Cu/Mg 12*b* sites in $I\bar{4}3d$ into a 4*b* and an 8*d* site in $I\bar{4}2d$. By assigning Mg to the 4*b* site and Cu to the 8*d* site, we built a model structure with the composition of $Ba_6(Cu_2Mg)Sn_4S_{16}$. The details of the model structure of $Ba_6(Cu_2Mg)Sn_4S_{16}$ are summarized in **Table S5**. The electronic band structures and density of states (DOS) curves of the $Ba_6Cu_3Sn_4S_{16}$ and $Ba_6(Cu_2Mg_1)Sn_4S_{16}$ model structures were calculated with first-principle DFT calculations using the Vienna Ab Initio Software Package (VASP).[57-60] Pseudopotentials generated with the projector augmented-wave (PAW) method[61] were employed. The Perdew-Burke-Ernzerhof (PBE) generalized gradient approximation[62] was employed to treat the electronic exchange-correlation. A 5 × 5 × 5 Monkhorst mesh[63] was used to sample the 1st Brillouin zones. The energy cutoff of the plane wave basis set is 295.4 eV. To confirm the electronic structures calculated from VASP, the DOS of $Ba_6Cu_3Sn_4S_{16}$ were calculated by TB-LMTO-ASA[64,65], which exhibited results consistent with the DOS calculated with VASP (*vide infra*). The chemical bonding characteristics of $Ba_6Cu_3Sn_4S_{16}$ were studied through electron localization function (ELF) and crystal orbital Hamilton population (COHP) calculations implemented in TB-LMTO-ASA [64, 65]. The same model structure of $Ba_6(Cu_2Mg)Sn_4S_{16}$ were utilized to estimate the optical properties of $Ba_6(Cu_{1.9}Mg_{1.1})Sn_4S_{16,}$ which were calculated based on ab initio calculations implemented in the CASTEP package through DFT [66]. The generalized gradient approximation (GGA) [67] was adopted, and the

Perdew−Burke−Ernzerhof (PBE) [68] function was chosen to calculate the exchange-correlation potential, with an energy cutoff of 900 eV. The numerical integration of the Brillouin zone was performed using a 2 × 2 × 2 Monkhorst−Pack k-point sampling. The geometry optimizations were applied prior to property calculations. Norm-conserving pseudopotentials were employed.

^{119}Sn Solid State NMR

All solid-state NMR experiments were performed on a Bruker wide-bore 9.4 T ($\nu_0(^1H) = 400$ MHz) NMR spectrometer equipped with a Bruker Advance III HD console and a Bruker 2.5 mm broadband HXY magic angle spinning (MAS) probe configured in ^{1}H-^{119}Sn-^{15}N mode. ^{1}H chemical shifts were referenced to tetramethylsilane by using adamantane ($\delta_{iso}(^1H) = 1.82$ ppm) as a secondary chemical shift standard. ^{119}Sn chemical shifts were indirectly referenced to the established chemical shift scale ($SnMe_4$, $\delta_{iso}(^{119}Sn) = 0$ ppm) using the previously published relative NMR frequencies.[69] ^{119}Sn SSNMR spectra were obtained with spin echo pulse sequences at a MAS rate of 25 kHz, with 71 kHz rf pulses, recycle delays of 1 s, and with 16,384 scans. 100 kHz ^{1}H rf field SPINAL-64 heteronuclear decoupling[70] was applied during signal acquisition. Analytical simulations of MAS ^{119}Sn solid-state NMR spectra were performed in the solid lineshape analysis (SOLA) module v3.6.3 included in the Bruker Topspin v3.6 software. The CASTEP program[71] was used to calculate ^{119}Sn chemical shielding tensor parameters using the Materials Studio 2018 environment (version 18.1.0.2017). All calculations used the Perdew−Burke−Ernzerhof (PBE)[62] generalized gradient approximation function and ultrasoft pseudopotentials, both generated on the fly.[72] All atomic positions were optimized, and P_1 symmetry was imposed on the unit cell prior to performing the NMR calculations. The NMR calculations were performed using the GIPAW method as implemented in CASTEP [72, 73].

Results and Discussion

Correct structure model

The $II_6I_4V_4Ch_{16}$(II=Sr, Ba; I=Li, Cu, Ag; IV=Ge, Sn; Ch=S, Se) family of compounds are isostructural and crystallize in the $Ba_6Ag_4Sn_4S_{16}$ [49] structure type. Previous single-crystal X-ray diffraction structures of these materials show that the structures and compositions are quite complex, with partial occupancy of several positions. For $Ba_6Ag_{4-x}Sn_4S_{16}$, there are two interstitial Ag atomic positions (occupancy of 0.07-0.16) close to the central Ag atoms (occupancy of 0.74-0.86), which results in variable chemical formulas of $Ba_6Ag_{3.41}Sn_4S_{16}$, $Ba_6Ag_{3.94}Sn_{4.02}S_{16}$, and $Ba_6Ag_4Sn_4S_{16}$.[49] $Ba_6Ag_{3.41}Sn_4S_{16}$ and $Ba_6Ag_{3.94}Sn_{4.02}S_{16}$ are not charge-balanced. A similar situation was also reported in $Sr_6Ag_4Sn_4S_{16}$. Within $Sr_6Ag_4Ge_4S_{16}$, there is only one interstitial Ag atomic position (occupancy of 0.333) neighbor to the central Ag atoms (occupancy of 0.667). A more complex situation was discovered in $Sr_6(Ag_{(4-y)}Sn_{(y/4)})(SnS_4)_4$, where two interstitial Ag atomic positions are close to the central Ag/Sn mixed atomic position.[43,45]

Here, during the refinement of the single crystal X-ray structure of $Ba_6(Cu_{2.9}Sn_{0.4})Sn_4S_{16}$, one interstitial atomic position was found as shown in **Figure 2a**. The connectivity between the interstitial atom and the center Cu1 is listed in **Figure 2d**. The interstitial atom is separated from the center Cu1 atom by 2.3 Å with an occupancy of 0.09 (3). Our initial assignment of the interstitial atom was as the Cu3 atom, which results in a chemical formula of $Ba_6Cu_{3.3}Sn_4S_{16}$. However, from electron counting and assuming the following oxidation states, $(Ba^{2+})_6(Cu^{+})_{3.3}(Sn^{4+})_4(S^{2-})_{16}$, a composition of $Ba_6Cu_{3.3}Sn_4S_{16}$ would be electron deficient and hence would be expected to be highly conductive. But, property measurements show that $Ba_6(Cu_{2.9}Sn_{0.4})Sn_4S_{16}$ is an electron-precise semiconductor (*vide infra*). Therefore, a structure

model featuring an interstitial Cu atom seems unlikely. Consequently, we considered the possibility of assigning the interstitial atom as Sn (occupancy of 0.07(1)), resulting in a chemical formula $Ba_6(Cu_{2.9}Sn_{0.4})Sn_4S_{16}$. Considering the accuracy of X-ray diffraction for determining composition and property measurements, we believe that the true composition is the nearly charge-balanced $(Ba^{2+})_6(Cu^{+})_{2.9}(Sn^{4+})_{4.4}(S^{2-})_{16}$. Indeed, the chemical ratio determined by EDX was $Ba_6Cu_{3.3(1)}Sn_{4.3(1)}S_{13.8(1)}$, which agrees well with single crystal X-ray diffraction refinement result of $Ba_6(Cu_{2.9}Sn_{0.4})Sn_4S_{16}$ (**Table S4**).

^{119}Sn solid-state NMR spectroscopy was employed to verify the structure model of $Ba_6(Cu_{2.9}Sn_{0.4})Sn_4S_{16}$, which is shown in **Figure 2b**. There are two observable ^{119}Sn NMR signals resonating at ca. −16.9 ppm and −25.7 ppm, respectively, with the integral ratio of ~ 1:1.5 (**Figure 2b)**. We assign both of these signals to the fully occupied Sn1 positions and believe that NMR signals are not directly observed for the partially occupied interstitial Sn2 atoms. First, the interstitial Sn2 are much more dilute than Sn1. The interstitial Sn2 tin atoms (0.07 occupancy × 24 Wyckoff number = 1.68 atoms per unit cell) should have NMR signals with approximately 10 times less intensity than Sn1 (16 atoms per unit cell), assuming similar relaxation constants for both sites. Furthermore, the interstitial Sn atoms reside in a distorted tetrahedral position with Sn-S bond lengths of 2.52 or 2.97 Å (two of each), while fully occupied Sn atoms reside in nearly tetrahedral environments which have three Sn-S bond lengths of 2.39 Å and one Sn-S bond length of 2.36 Å. Therefore, it is also possible that Sn2 atoms may give rise to ^{119}Sn NMR signals with significant chemical shift anisotropy, further hindering observation of these NMR signals. With the differences in Sn-S bond lengths and S-Sn-S bond angles for Sn1 and Sn2, it is also possible that there is a significant difference in isotropic ^{119}Sn chemical shifts as well. The observation of two Sn1 NMR signals likely reflects the disorder in the structure. Each Sn1 atom has three potential

Sn2 atoms (3.30 Å Sn1-Sn2 distance) and additional six Sn2 atoms that are 5.38 Å (three Sn2) and 5.47 Å (three Sn2) away, respectively. With an occupancy of 0.069 for Sn2, 52.5% of Sn1 atoms will have no adjacent Sn2 atom within the 9 nearest positions while the other 47.5% will have at least one adjacent Sn2 atom (**Table S6 and Table S7**). The normalized integrated intensity of the two peaks in the ^{119}Sn NMR spectrum is ~ 1.5:1. Therefore, the lower frequency more intense peak is assigned to Sn1 without the adjacent Sn2 atom, while the higher frequency peaks are assigned to a Sn1 adjacent to at least one single Sn2 atom.

With Mg atoms replacing Cu atoms in $Ba_6(Cu_2Mg)Sn_4S_{16}$, the interstitial atomic position disappeared (**Figure 2c**) as the red circle highlights. The Cu atoms, jointly mixed with Mg atoms, are located in the center of a tetrahedron with Cu/Mg-S distances slightly expanded to 2.43 Å (**Figure 2e**). The exclusion of an interstitial atomic position was observed in $Ba_6(Cu_xZ_y)Sn_4S_{16}$(Z=Mg, Mn, Zn, Cd, In, Bi) compounds. Hence the structure of $Ba_6(Cu_{2.9}Sn_{0.4})Sn_4S_{16}$ is different from $Ba_6(Cu_xZ_y)Sn_4S_{16}$(Z=Mg, Mn, Zn, Cd, In, Bi). There is an interstitial atomic position occupied by Sn in $Ba_6(Cu_{2.9}Sn_{0.4})Sn_4S_{16}$. The same interstitial atomic position was absent in $Ba_6(Cu_xZ_y)Sn_4S_{16}$(Z=Mg, Mn, Zn, Cd, In, Bi), where Z (Z= Mg, Mn, Zn, Cd, In, Bi) atoms jointly occupy the Cu atomic positions.

^{119}Sn solid-state NMR spectroscopy was also employed to verify the structure models of $Ba_6(Cu_{1.9}Mg_{1.1})Sn_4S_{16}$ and $Ba_6(Cu_{2.2}Mn_{0.8})Sn_4S_{16}$. All solid-state NMR spectra of the examined compounds (Cu, Cu/Mg and Cu/Mn) have similar ^{119}Sn chemical shift for the primary SnS_4 tetrahedron, despite the different combinations of $[CuS_4]$/$[MgS_4]$/$[MnS_4]$ and Ba neighbors. There are multiple observable ^{119}Sn NMR signals in the NMR spectra because there is likely a random siting of Cu/Mg and Cu/Mn in the neighboring $[(Cu/Mg)S_4]$ or $[(Cu/Mg)S_4]$ tetrahedra. Due to the roughly 66% atomic ratio of Cu and 33% atomic ratio of Mg/Mn, the probabilities of having

adjacent Cu_3, Cu_2Mg/Cu_2Mn, $CuMg_2/CuMn_2$ and Mg_3/Mn_3 tetrahedra is $p(Cu_3) = 0.287$, $p(Cu_2Mg/Cu_2Mn) = 0.444$, $p(CuMg_2/CuMn_2) = 0.222$, and $p(Mg_3/Mn_3) = 0.037$, respectively (**Table 1 and Table S8**). Fitting the ^{119}Sn NMR spectra to mixed Lorentzian/Gaussian peaks yields integrated intensities that show reasonable agreement with the calculated probabilities for both $Ba_6(Cu_xZ_y)Sn_4S_{16}$(Z=Mg, Mn) compounds. Note a 5th peak at ca. −47.6 ppm was needed in the fit of the ^{119}Sn NMR spectrum of the Mg compound.

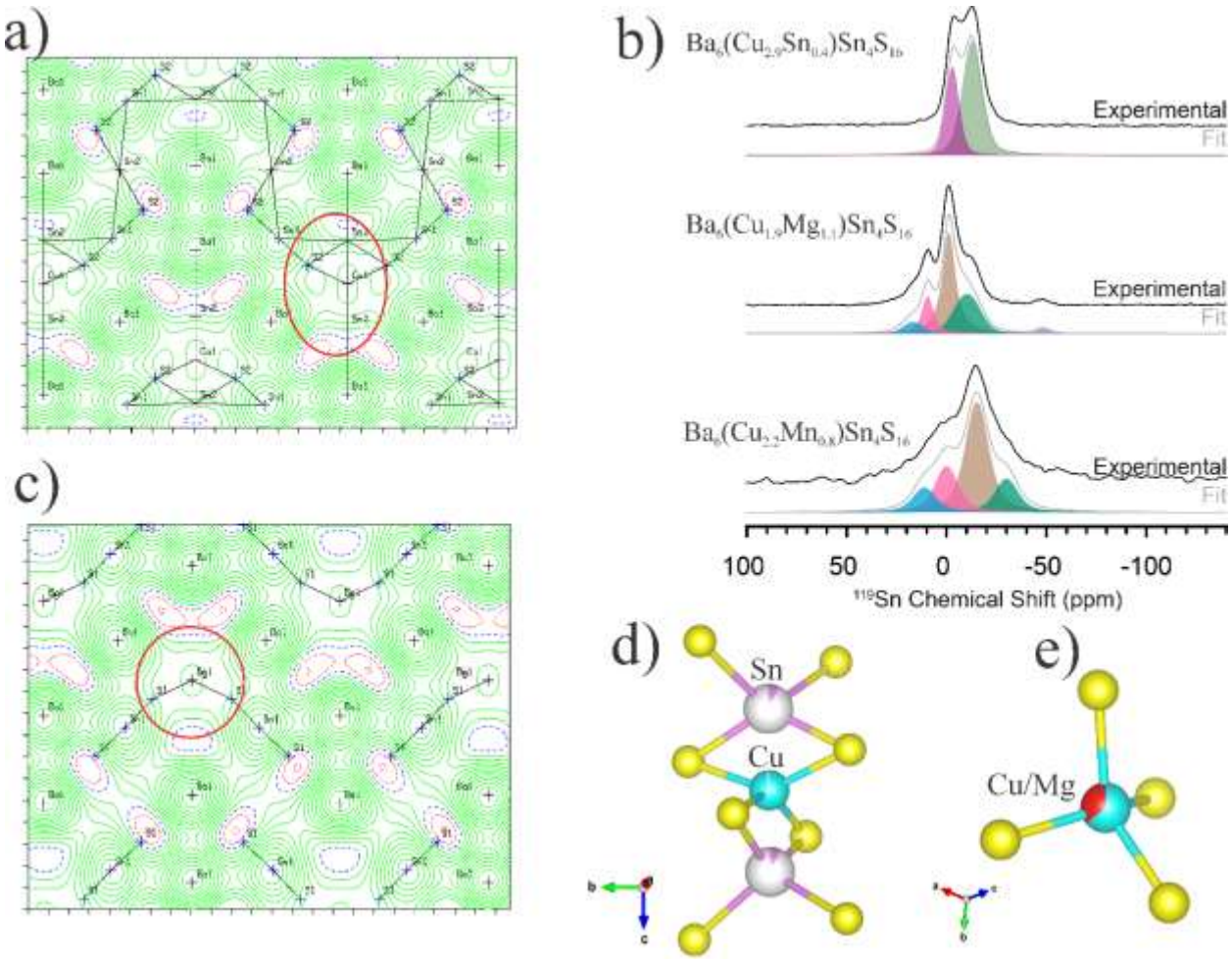

Figure 2. a) and c) Contoured section of the electron density difference map for $Ba_6(Cu_{2.9}Sn_{0.4})Sn_4S_{16}$ and $Ba_6(Cu_{1.9}Mg_{1.1})Sn_4S_{16}$, respectively. Contour lines, solid for positive values and dashed for zero or negative values, are drawn with 0.15 e/Å^3 increments. The red circles

highlight the interstitial Sn atoms in $Ba_6(Cu_{2.9}Sn_{0.4})Sn_4S_{16}$ and $(CuMg)S_4$ units in $Ba_6(Cu_{1.9}Mg_{1.1})Sn_4S_{16}$; b) 1D direct excitation ^{119}Sn spin echo spectra of $Ba_6(Cu_{2.9}Sn_{0.4})Sn_4S_{16}$, $Ba_6(Cu_{1.9}Mg_{1.1})Sn_4S_{16}$, and $Ba_6(Cu_{2.2}Mn_{0.8})Sn_4S_{16}$ recorded at 9.4 T. The magic angle spinning (MAS) rate is 25 kHz. The solid lines represent the experimental spectra, while the dashed lines are analytical simulations of the chemical shift anisotropy (CSA) powder patterns with Lorentz broadening; d): the connectivity between interstitial Sn atoms and $[CuS_4]$ tetrahedra; e) the $[(Cu/Mg)S_4]$ tetrahedral in $Ba_6(Cu_{1.9}Mg_{1.1})Sn_4S_{16}$. Cu: blue, Sn: red, Mg: orange, S: yellow.

Table 1. NMR Fitting Parameters and Relative Populations for the 1D ^{119}Sn Spin Echo Spectra of $Ba_6(Cu_xZ_y)Sn_4S_{16}$(Z=Mg, Mn)

Compounds	Neighboring tetrahedra species	$\delta_{iso}(^{119}Sn)$ (ppm)	Population determined from analytical simulation of experimental spectra (%)	Population determined from theoretical analysis (%)
$Ba_6(Cu_2Mg)Sn_4S_{16}$	Cu_3	−10.0	28.7	29.6
	Cu_2Mg	−1.0	48.0	44.4
	$CuMg_2$	10.0	15.0	22.2
	Mg_3	17.0	8.3	3.7
$Ba_6(Cu_2Mn)Sn_4S_{16}$	Cu_3	−30.0	17.6	29.6
	Cu_2Mn	−15.2	46.7	44.4
	$CuMn_2$	0	25.1	22.2
	Mn_3	11.1	10.6	3.7

Crystal growth and phase homogeneity

High quality mm-sized crystals of $Ba_6(Cu_xZ_y)Sn_4S_{16}$(Z=Mg, Mn, Zn, Cd, In, Bi, Sn) were grown in KI salt flux. Various fluxes such as KCl/NaCl and $BaCl_2$ only generated small yields of the target compounds. The vapor transport reaction utilizing I_2 as a transport agent also failed. During the crystal growth process, the ratio of reactants was adjusted to probe for better crystal yields. Using the Ba-Cu-Mg-Sn-S system as an example, Ba/Cu/Mg/Sn/S with ratios of 6/2/2/4/16, 6/3/2/4/16, and 6/2/1/4/16 were mixed with KI to grow crystals. SXRD revealed a constant ratio of Ba/Cu/Mg/Sn/S ≈ 6/2/1/4/16, which can achieve the charge balance of $(Ba^{2+})_6(Cu^{+})_2(Mg^{2+})_1$

$(Sn^{4+})_4(S^{2-})_{16}$. Similar situations were observed for other metal dopants. Herein we conclude that there is little to no phase width existing in the $Ba_6(Cu_xZ_y)Sn_4S_{16}$(Z=Mg, Mn, Zn, Cd, In, Bi, Sn) system. Another proof of this statement is the narrow peaks of the powder X-ray diffraction results (**Figure 1** and **Figure S1**).

Crystal structure

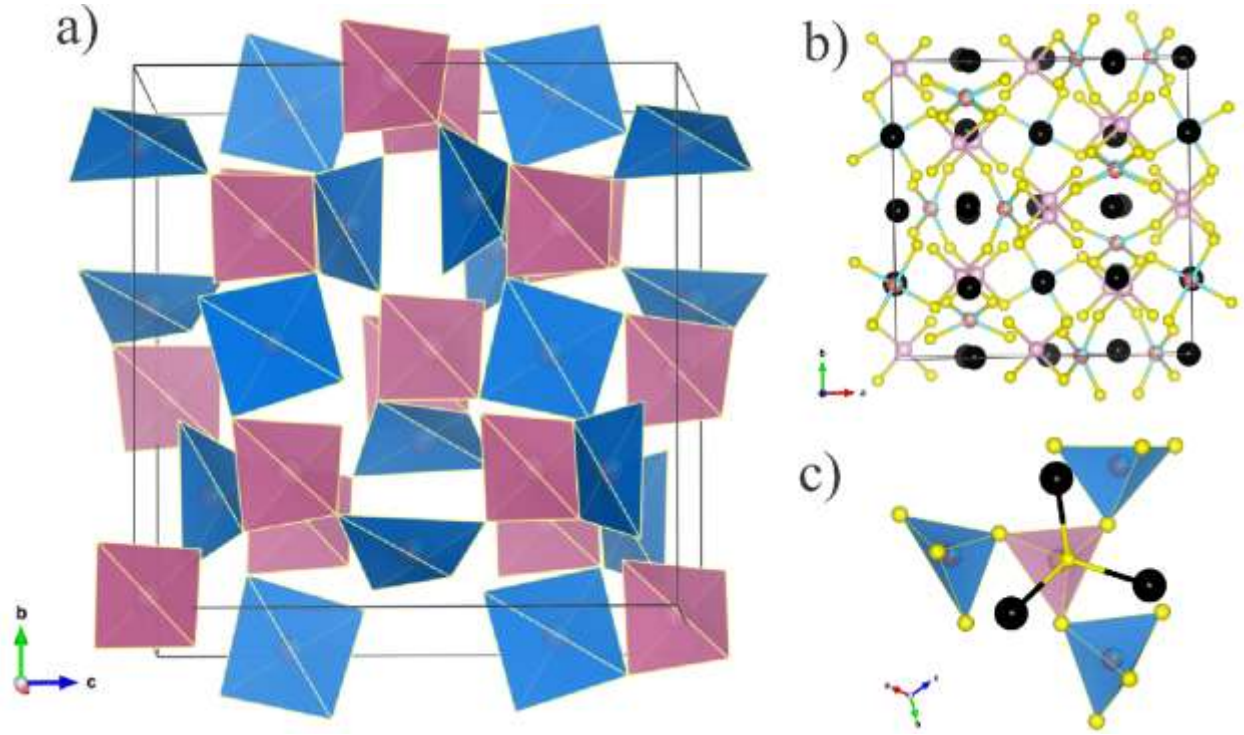

Figure 3. a) Polyhedral structure view of $Ba_6(Cu_{1.9}Mg_{1.1})Sn_4S_{16}$ along the [100] axis emphasizing the 3D network constructed by [SnS_4] tetrahedra (pink) and [(Cu/Mg)S_4] tetrahedra (blue), Ba cations omitted for clarity; b) ball-stick structure view of $Ba_6(Cu_{1.9}Mg_{1.1})Sn_4S_{16}$ along the [001] axis; c) the connectivity between [SnS_4] tetrahedra (blue) and [(Cu/Mg)S_4] tetrahedra (pink). Ba: black, Sn: pink, Cu: blue, Mg: red, S: yellow.

$Ba_6(Cu_xZ_y)Sn_4S_{16}$(Z=Mg, Mn, Zn, Cd, In, Bi) compounds are isostructural and crystallize in the $Ba_6Ag_4Sn_4S_{16}$ [49] structure type with the noncentrosymmetric cubic space group $I\bar{4}3d$ (No. 220). $Ba_6(Cu_{2.9}Sn_{0.4})Sn_4S_{16}$ also crystallizes in cubic space group $I\bar{4}3d$ (No. 220). With the removal of the low occupancy Sn atomic position, $Ba_6(Cu_{2.9}Sn_{0.4})Sn_4S_{16}$ is found to be isostructural to

$Ba_6(Cu_xZ_y)Sn_4S_{16}$(Z=Mg, Mn, Zn, Cd, In, Bi) compounds. Hence, the discussion of the structure will mainly be focused on $Ba_6(Cu_xZ_y)Sn_4S_{16}$(Z=Mg, Mn, Zn, Cd, In, Bi) compounds.

$Ba_6(Cu_{1.9}Mg_{1.1})Sn_4S_{16}$ is selected to present the structure of the $Ba_6(Cu_xZ_y)Sn_4S_{16}$(Z=Mg, Mn, Zn, Cd, In, Bi) compounds. The Wyckoff sequence of $Ba_6(Cu_{1.9}Mg_{1.1})Sn_4S_{16}$ is edc^2a^2 with a Pearson symbol *cI*128. In $Ba_6(Cu_{1.9}Mg_{1.1})Sn_4S_{16,}$ one unique Ba atom resides at Wyckoff site 24*d*, one Sn atom resides at Wyckoff site 16*c*, and two S atoms occupy Wyckoff sites 48*e* and 16*c*, which are all full occupancy. Cu jointly occupies the Wyckoff position 12*a* with Mg with occupancies of 67% and 33%, respectively. Selected crystal data and parameters are listed in **Table S1**. The atomic coordination and selected bond distances are listed in **Table S2** and **Table S3** respectively.

$Ba_6(Cu_xZ_y)Sn_4S_{16}$(Z=Mg, Mn, Zn, Cd, In, Bi) compounds belong to the $II_6I_4V_4Ch_{16}$(II=Sr, Ba, I=Li, Cu, Ag, IV=Ge, Sn, Ch=S, Se) family. [42-51] There were 30 compounds discovered in the $II_6I_4V_4Ch_{16}$family so far. [42-51] The number of compounds of the $II_6I_4V_4Ch_{16}$ family was greatly expanded via introducing mixed occupancy at the Li/Cu/Ag atomic positions, where the monovalent metals are replaced by divalent metals. The flexible combination of elements coupled with the mixed occupancy at the Wyckoff position 12*a* accounts for the large number of compounds in the $II_6I_4V_4Ch_{16}$ family. In this work, we demonstrated that the chemical flexibility of the $II_6I_4V_4Ch_{16}$ family can be further expanded via replacing monovalent metals by trivalent metals. Many previous works have summarized the structure of the $II_6I_4V_4Ch_{16}$ family. Herein, we will briefly summarize the structure of $Ba_6(Cu_{1.9}Mg_{1.1})Sn_4S_{16}$ with emphasis of the mixed occupancy between Cu atoms and Mg atoms. The polyhedral structure view and ball-stick structure view of $Ba_6(Cu_{1.9}Mg_{1.1})Sn_4S_{16}$ are presented in **Figure 3a** and **Figure 3b,** respectively. The three-dimensional (3D) framework of $Ba_6(Cu_{1.9}Mg_{1.1})Sn_4S_{16}$ is constructed by $[SnS_4]$ tetrahedra and $[(Cu/Mg)S_4]$ tetrahedra via corner sharing, where the Ba^{2+} cations fill the empty

spaces and balance the charge. The connectivity between [SnS_4] tetrahedra and [(Cu/Mg)S_4] tetrahedra are highlighted in **Figure 3c**. As shown in **Figure 3c**, three of four vertices of [SnS_4] tetrahedra are shared with [(Cu/Mg)S_4] tetrahedra. The fourth vertex of [SnS_4] tetrahedra is surrounded by three Ba^{2+} cations. All vertices of [(Cu/Mg)S_4] tetrahedra are shared by [SnS_4] tetrahedra. This mixed occupancy between Mg and Cu enlarges the Cu/Mg-S bonds to 2.426 (3) Å, which is longer than Cu-S bonds in $Ba_6(Cu_{2.9}Sn_{0.4})Sn_4S_{16}$ (2.399(4) Å). The trivalent dopants Bi and In slightly enlarge the $(Cu/Z\text{-}S)_{Z=Bi\ or\ In}$ bonds to 2.414 (2) Å. The Cu/Mn-S bonds are longer than other Cu/Z-S bonds of 2.434 (3) Å. The Sn atoms fully occupy the center of [SnS_4] tetrahedra with a bond distance of 2.345(5)-2.403(3) Å, which are close to the Sn-S bonds of 2.363(7)-2.396(4) Å within $Ba_6(Cu_{2.9}Sn_{0.4})Sn_4S_{16}$. The Sn-S bonds of $Ba_6(Cu_xZ_y)Sn_4S_{16}$ (Z=Mg, Mn, Zn, Cd, In, Bi) compounds reside in a very narrow range of 2.342(4)-2.407(3) Å, which are comparable to many tin-sulfides such as $BaAg_2SnS_4$(2.388 Å) [74], $RbBa_2SnS_4Cl$ (2.341-2.376 Å) [75], $Ba_7Sn_3S_{13}$ (2.338-2.410 Å) [76], Li_2MnSnS_4 (2.387-2.395 Å) [28], and $Ba_8Sn_4S_{15}$ (2.363-2.615 Å) [77], etc.

Electronic structures

To understand the electronic structures of $Ba_6(Cu_{2.9}Sn_{0.4})Sn_4S_{16}$ and $Ba_6(Cu_{1.9}Mg_{1.1})Sn_4S_{16}$, two hypothesized structural models, $Ba_6Cu_3Sn_4S_{16}$ and $Ba_6(Cu_2Mg)Sn_4S_{16}$, were built. Two different methods, VASP and TB-LMTO-ASA, were employed to study the electronic structures of $Ba_6Cu_3Sn_4S_{16}$, which generated consistent results and are shown in **Figure 4 top** and **Figure S5.** $Ba_6Cu_3Sn_4S_{16}$ is predicated to be electron deficient. The Fermi level (0 eV) is located within a narrow sharp peak in DOS (**Figure 4 top** and **Figure S5**). Integrating the DOS reveals that elevating the Fermi level to the band gap requires one more electron per $Ba_6Cu_3Sn_4S_{16}$ unit. The electron deficiency also indicates the importance of the interstitial Sn atoms, which can compensate the electron deficiency and raise the Fermi level up to the bandgap. The partial density

of states analysis confirmed that the *3d* orbitals of Cu atoms and *3p* orbitals of S atoms dominantly contribute to the states below the Fermi level. The Ba (*6s*) orbitals have certain contributions to the states around the Fermi level, where the Sn atoms have minimum contributions. This indicates that the upper edge of the valence band (the "frontier orbitals") is mainly contributed by the Cu and S orbitals in $Ba_6Cu_3Sn_4S_{16,}$ indicating that the [CuS_4] tetrahedra are important to the stability and optical properties of $Ba_6Cu_3Sn_4S_{16}$, which was confirmed by the optical properties' calculations (*vide infra*).

The band structures and DOS of $Ba_6(Cu_2Mg)Sn_4S_{16}$ are similar to $Ba_6Cu_3Sn_4S_{16}$. Except that $Ba_6(Cu_2Mg)Sn_4S_{16}$ is a charge-balanced compound and predicated to be a direct bandgap semiconductor with the Fermi level (0 eV) located within the bandgap. The calculated bandgap of $Ba_6(Cu_2Mg)Sn_4S_{16}$ is 1.2 eV, which is lower than the measured value of 2.4 eV via UV-Vis spectrum test. The bandgap calculated by the GGA functional method generated comparable results of 1.96 eV (**Figure S6**). Similar to $Ba_6Cu_3Sn_4S_{16}$, Cu (*3d)* orbitals, and S (*3p)* orbitals contribute the most to the states below the Fermi level (0 eV). The Ba, Mg, and Sn also contribute to these states below the Fermi level (0 eV) but to a less extent. At the bottom of the conduction band, Ba (6s) orbitals, Sn (*5p)* orbitals, and S (*3p)* orbitals have major contributions. The calculated partial density of states of $Ba_6(Cu_2Mg)Sn_4S_{16}$ from CASTEP (**Figure S7**) agrees well with **Figure 4, bottom,** simulated by VASP. The electronic structure analysis of both $Ba_6Cu_3Sn_4S_{16}$ and $Ba_6(Cu_2Mg)Sn_4S_{16}$ indicates that [CuS_4] tetrahedra and [SnS_4] tetrahedra are important to the stability and optical properties of $Ba_6(Cu_xZ_y)Sn_4S_{16}$(Z=Mg, Mn, Zn, Cd, In, Bi, Sn) compounds.

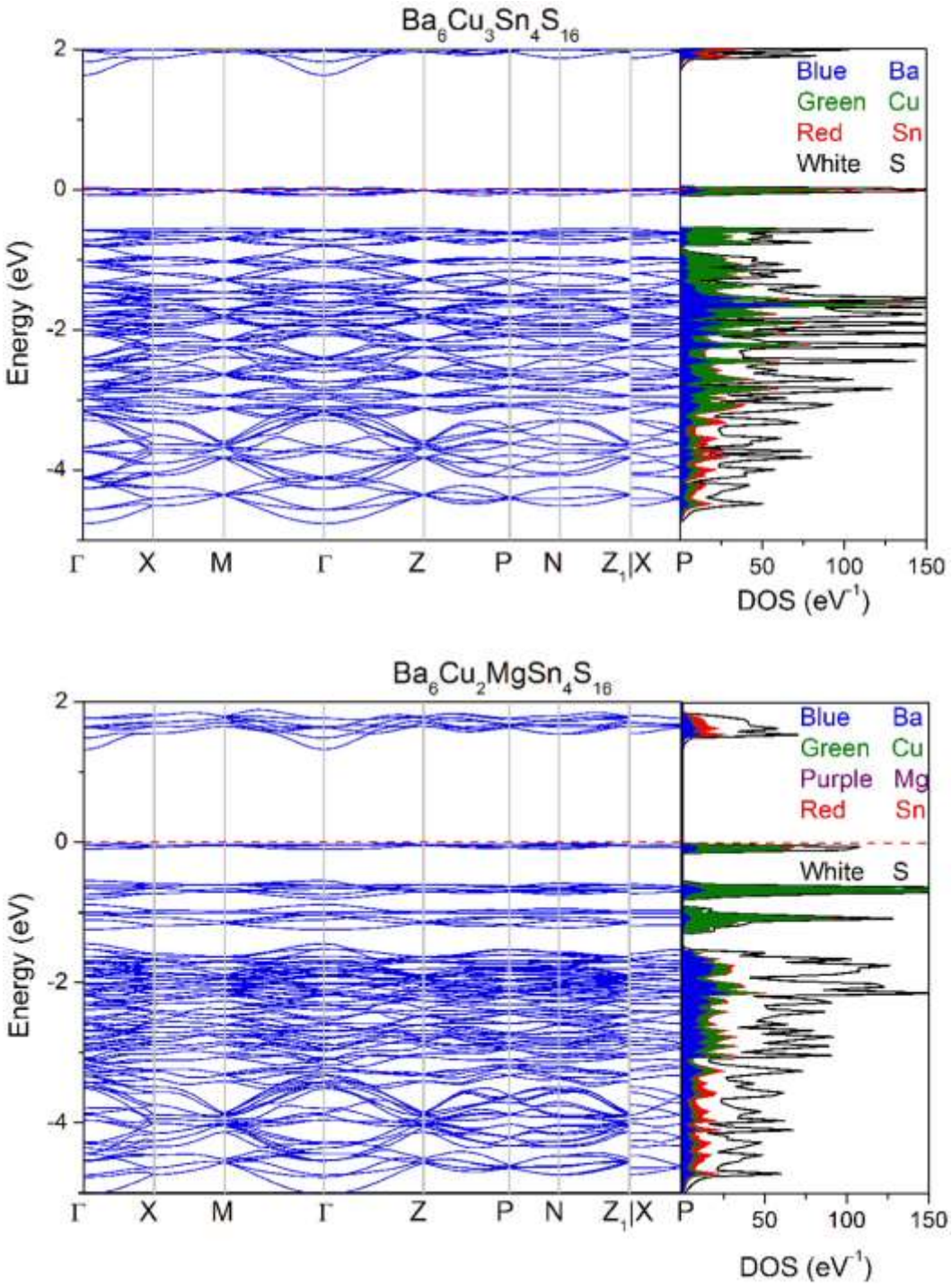

Figure 4. (Top) band structure, density of states (DOS), and partial density of states (PDOS) of $Ba_6Cu_3Sn_4S_{16}$, (bottom) band structure, density of states (DOS), and partial density of states (PDOS) of $Ba_6(Cu_2Mg)Sn_4S_{16}$.

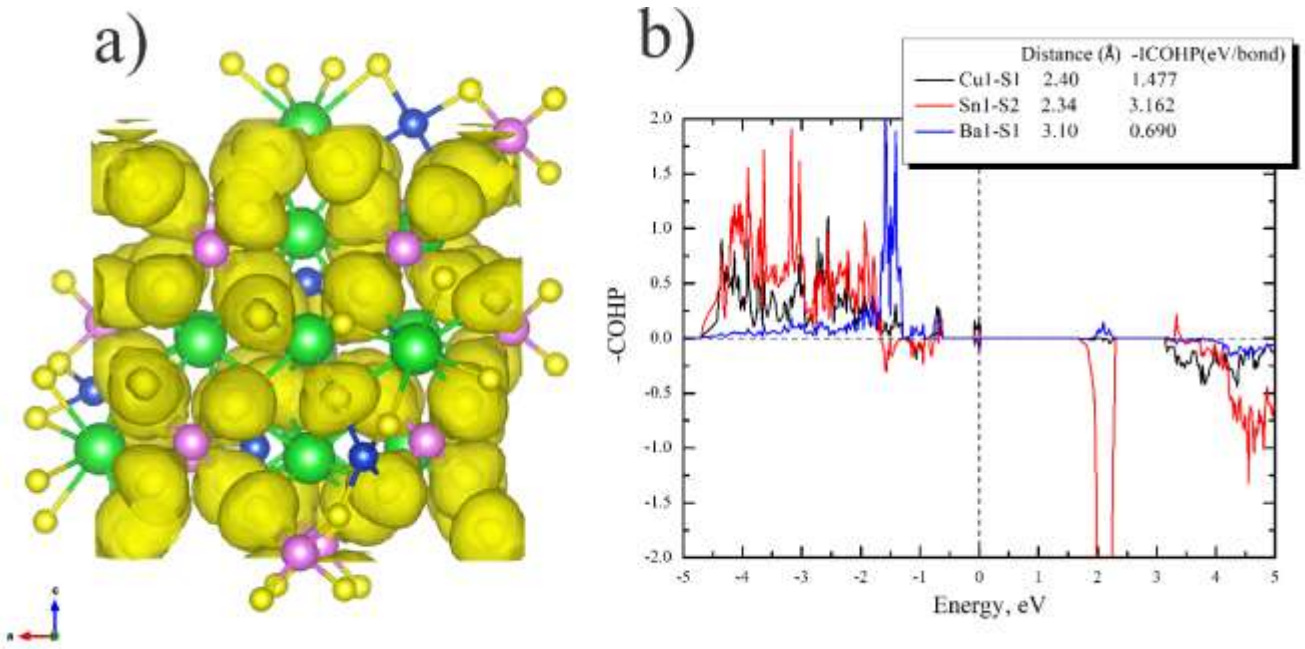

Figure 5. (a) 3D isosurfaces of the electron localization function (ELF) for $Ba_6Cu_3Sn_4S_{16}$ with η=0.65, Ba: green, Cu: blue, Sn: pink, S: yellow. (b) Crystal orbital Hamilton population (COHP) analyses of the selected Cu−S interactions, Sn−S interactions, and Ba−S interactions.

The bonding pictures within $Ba_6Cu_3Sn_4S_{16}$ were studied by ELF simulations coupled with COHP calculations, which are shown in **Figure 5**. There are no ELF maxima surfaces capping the Ba atoms and existing between Ba-S interactions, which indicate the dominantly ionic characteristics of Ba-S interactions. The Ba-S interactions of 3.10 Å is predicated by COHP calculations to exhibit non-negligible bonding characters with –ICOHPs of 0.690 eV/bond (**Figure 5b**). A similar situation was observed for the Cu-S interactions. No ELF maxima surfaces surround the Cu atoms and locate between Cu-S interactions, where the ELF isosurfaces are mainly surrounding the S atoms. Our recent study about Cu-Se interactions within $Cu_{2.83}Bi_{10}Se_{16}$ shows comparable results [78]. The COHP calculation confirms the strong bonding nature of Cu-S interactions. The –ICOHPs of 2.40 Å Cu-S interactions are 1.477 eV/bond. Combing ELF and COHP results, the strong Cu-S bonds exhibit mainly ionic characteristics with Cu being "cationic" and S being "anionic". When

moving to look at Sn-S interactions, a different story appears. There are apparent attractors (ELF maxima between atoms) between Sn and S, making the ELF maxima surfaces a "pear" shape [15]. The absence of attractors capping Sn atoms also confirmed the oxidation state of Sn is +4 [15]. The 2.34 Å Sn-S interactions show the strongest bonding character with –ICOHPs of 3.162 eV/bond. The strong Sn-S bonds exhibit mainly covalent character. In summary, $[CuS_4]$ tetrahedra built with ionic Cu-S bonds and $[SnS_4]$ tetrahedra, consisting of covalent Sn-S bonds, significantly contribute to the structure stability and optical properties of $Ba_6Cu_3Sn_4S_{16}$. Further DFT calculations on $Ba_6(Cu_2Mg)Sn_4S_{16}$ also verified the importance of $[CuS_4]$ tetrahedra and $[SnS_4]$ tetrahedra on its structure stability and optical properties (*vide infra*).

Linear and nonlinear optical properties

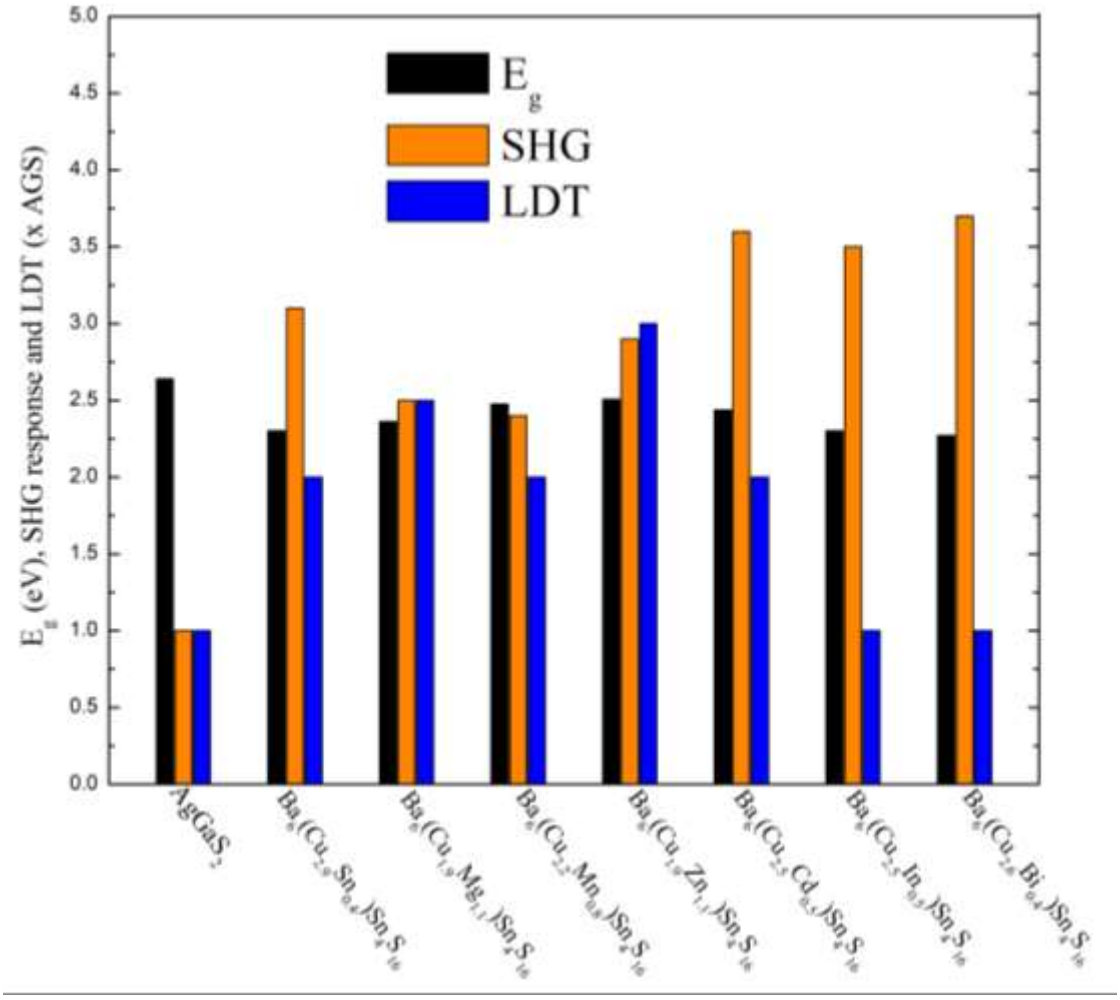

Figure 6. A summary of comparison between $AgGaS_2$ and $Ba_6(Cu_xZ_y)Sn_4S_{16}$(Z=Mg, Mn, Zn, Cd, In, Bi, Sn) compounds in regard to bandgap (E_g), SHG intensity (2.09 μm, sample particle size of 38-55 μm), and LDT,.

The bandgaps of $Ba_6(Cu_xZ_y)Sn_4S_{16}$(Z=Mg, Mn, Zn, Cd, In, Bi, Sn) compounds were estimated by solid-state UV-Vis reflectance spectroscopy, which are shown in **Figure 6**. The Tauc plots were employed to estimate the direct and indirect bandgaps of $Ba_6(Cu_xZ_y)Sn_4S_{16}$(Z=Mg, Mn, Zn, Cd, In, Bi) compounds, which are shown in **Figure S2** and **Figure S3**. The bandgap of $Ba_6(Cu_{2.9}Sn_{0.4})Sn_4S_{16}$ is 2.3 eV. $Ba_6(Cu_{1.9}Zn_{1.1})Sn_4S_{16}$ shows the largest bandgap of 2.5 eV, while $Ba_6(Cu_2In_{0.5})Sn_4S_{16}$ has the smallest bandgap of 2.2 eV. The doping of divalent and trivalent metals at Cu atomic position slightly affects the linear optical properties and significantly influences the nonlinear optical properties of $Ba_6(Cu_xZ_y)Sn_4S_{16}$(Z=Mg, Mn, Zn, Cd, In, Bi)

compounds (*vide infra*). The IR transmission range is an important parameter for IR NLO materials. Current data acquisitions of IR transmission range were impeded by small crystal size. Growth of large crystals is ongoing to investigate more intrinsic properties of $Ba_6(Cu_xZ_y)Sn_4S_{16}$(Z=Mg, Mn, Zn, Cd, In, Bi, Sn) compounds.

The nonlinear optical properties of SHG intensity and LDT of $Ba_6(Cu_xZ_y)Sn_4S_{16}$(Z=Mg, Mn, Zn, Cd, In, Bi, Sn) compounds, compared with $AgGaS_2$, are summarized in **Figure 6**. As shown in **Figure S4**, $Ba_6(Cu_xZ_y)Sn_4S_{16}$(Z=Mg, Mn, Zn, Cd, In, Bi, Sn) compounds are not type-I phase-matching materials, the second harmonic generation intensity decreases with increasing particle size. Hence, the comparison of SHG intensity of $Ba_6(Cu_xZ_y)Sn_4S_{16}$(Z=Mg, Mn, Zn, Cd, In, Bi, Sn) compounds with $AgGaS_2$ crystals are based on samples of particle size of 38-55 μm. $Ba_6(Cu_{2.9}Sn_{0.4})Sn_4S_{16}$ exhibits a good SHG intensity of 2.3×AGS. As theory calculations predicted, the doping of metals at the Cu atomic position will significantly shift the optical properties of $Ba_6(Cu_xZ_y)Sn_4S_{16}$(Z=Mg, Mn, Zn, Cd, In, Bi) compounds. $Ba_6(Cu_{2.6}Bi_{0.4})Sn_4S_{16}$ exhibits the best SHG response of 3.6 × AGS. $Ba_6(Cu_{2.5}Cd_{0.5})Sn_4S_{16}$ and $Ba_6(Cu_{2.5}In_{0.5})Sn_4S_{16}$ also show comparable SHG performances to $Ba_6(Cu_{2.6}Bi_{0.4})Sn_4S_{16}$ of 3.2 ×AGS and 3.3×AGS, respectively. While the Mg, Zn, and Mn doping suppress the SHG performance of $Ba_6(Cu_{2.9}Sn_{0.4})Sn_4S_{16}$. Surprisingly, the $Ba_6(Cu_xZ_y)Sn_4S_{16}$(Z=Mg, Mn, Zn, Cd, In, Bi) system exhibits impressively high LDT. $Ba_6(Cu_{1.9}Zn_{1.1})Sn_4S_{16}$ shows a high LDT of 3× AGS. The LDT of $Ba_6(Cu_{1.9}Mg_{1.1})Sn_4S_{16}$ is about 2.5× AGS. The record holder of the LDT of the $II_6I_4V_4Ch_{16}$(II=Sr, Ba, I=Li, Cu, Ag, IV=Ge, Sn, Ch=S, Se) family is $Sr_6Li_2CdGe_4S_{16}$ of 20.63 × AGS with a bandgap of 3.8 eV [50]. There are many factors contributing to the LDT of crystalline solids. The LDT has two parts: dielectric LDT and thermal LDT [79]. The dielectric LDT is governed by (atomic density)/(n^2-1), where n is refractivity. The materials with narrow band gaps generally

have large refractivity values. The thermal LDT is proportional to CκS/αβ, where C is the heat capacity, κ is thermal conductivity containing contributions from carrier branches and phonon branches, S is damaging stress and is positively correlated with Young's modulus and shear modulus of the material, α is the absorption coefficient and β is the thermal expansion coefficient. Even the band gaps of $Ba_6(Cu_xZ_y)Sn_4S_{16}$(Z=Mg, Mn, Zn, Cd, In, Bi) compounds are close to or smaller than AGS, the LDTs of $Ba_6(Cu_xZ_y)Sn_4S_{16}$(Z=Mg, Mn, Zn, Cd, In, Bi) compounds are higher than AGS, which may originate from a higher thermal conductivity due to their cubic crystal structure or smaller absorption coefficients [79]. Two compounds with comparable bandgaps, such as $Sr_6Cu_4Sn_4S_{16}$ (E_g=2.1 eV) [43]and $Sr_6Ag_4Sn_4S_{16}$ (E_g=1.9 eV) [43], exhibit a lower LDT of 2×AGS and 2×AGS, respectively. $Ba_6(Cu_{1.9}Zn_{1.1})Sn_4S_{16}$ exhibits the best performance due to the excellent balance between SHG and LDT. The doping of divalent metals and trivalent metals at Cu atomic sites demonstrate the structural flexibility of the $II_6I_4V_4Ch_{16}$(II=Sr, Ba, I=Li, Cu, Ag, IV=Ge, Sn, Ch=S, Se) family and significantly shift their nonlinear optical properties. The mixed occupancy is beneficial in achieving good balance between SHG and LDT in $Ba_6(Cu_xZ_y)Sn_4S_{16}$(Z=Mg, Mn, Zn, Cd, In, Bi, Sn) compounds [80, 81].

DFT calculations for optical properties

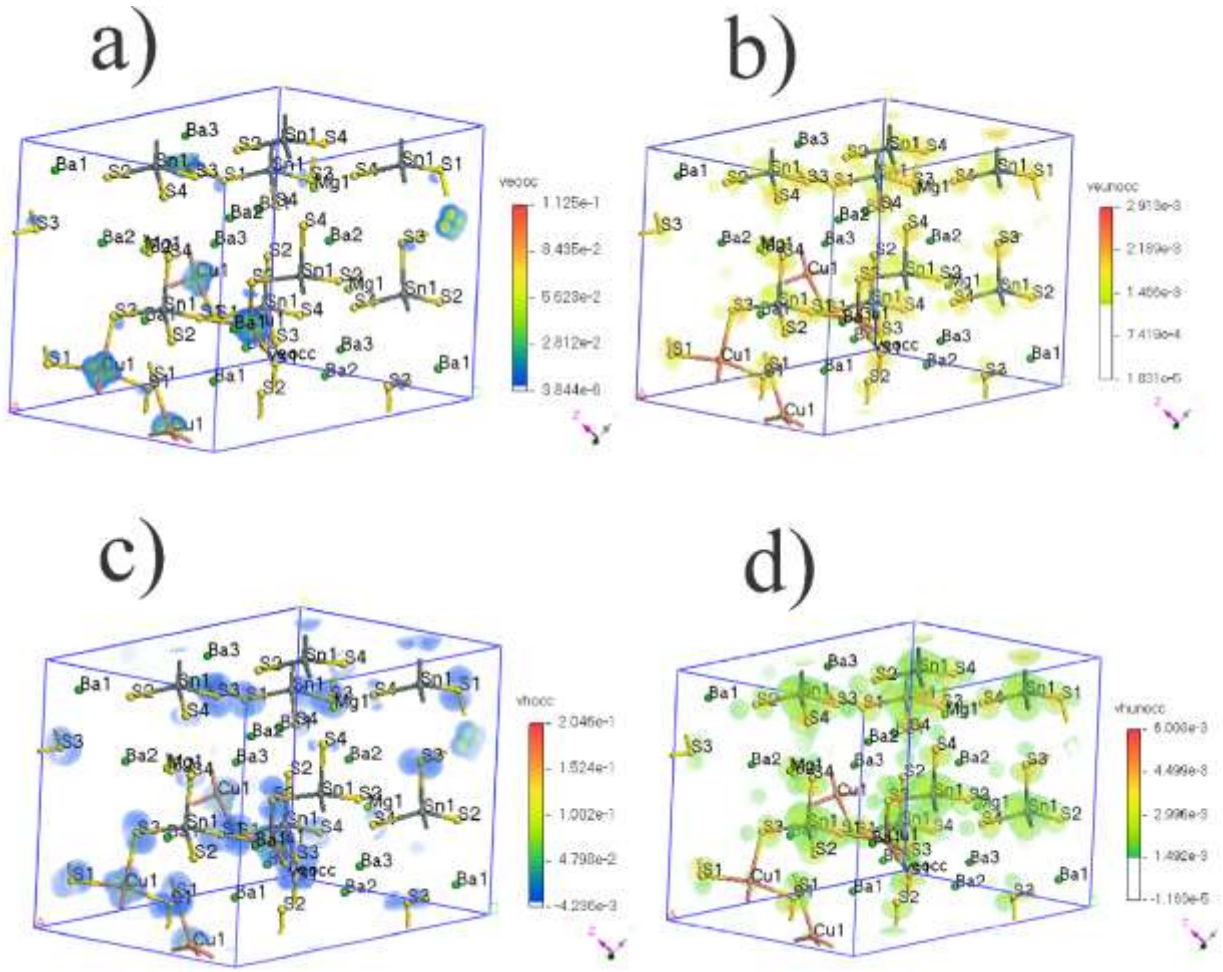

Figure 7. (a) SHG density of VE occupied states (veocc), (b) VE unoccupied states(veunocc), (c) VH occupied states (vhocc), and (d) VH unoccupied states (vhuocc) in $Ba_6(Cu_2Mg)Sn_4S_{16}$.

To better understand the origin of the nonlinear optical properties of $Ba_6(Cu_2Mg)Sn_4S_{16}$, DFT calculations were employed, which are shown in **Figure 7.** The superstructure model of $Ba_6(Cu_2Mg)Sn_4S_{16}$ is the same structure model used for the electronic structure analysis, which is listed in **Table S5**. The calculation of χ^{123} of $Ba_6(Cu_2Mg)Sn_4S_{16}$ is 18.572 pm/V, which predicts a moderate second harmonic generation response. The experimental SHG response tests confirmed the theory calculation results with the observed ~2.5 ×AGS SHG response (**Figure 6**). The analysis of occupied states and unoccupied states of VE and VH pointed out the critical roles of the $[CuS_4]$

tetrahedra's contribution to the second harmonic generation response of $Ba_6(Cu_2Mg)Sn_4S_{16}$. There are also significant contributions from $[SnS_4]$ tetrahedra. In this superstructure model of $Ba_6(Cu_2Mg)Sn_4S_{16}$, $[MgS_4]$ tetrahedra have negligible contribution to the SHG response. With Cu replaced by various metals, the NLO properties of $Ba_6(Cu_xZ_y)Sn_4S_{16}$(Z=Mg, Mn, Zn, Cd, In, Bi) compounds were significantly shifted (**Figure 6**). Hence, we can conclude that the $[CuS_4]$ tetrahedra and $[SnS_4]$ tetrahedra play an important role in the stability, chemical flexibility, and optical properties of $Ba_6(Cu_xZ_y)Sn_4S_{16}$(Z=Mg, Mn, Zn, Cd, In, Bi) compounds. All $Ba_6(Cu_xZ_y)Sn_4S_{16}$(Z=Mg, Mn, Zn, Cd, In, Bi) compounds exhibit non-phase-matchable behavior.

Conclusions

High quality crystals of seven noncentrosymmetric sulfides $Ba_6(Cu_xZ_y)Sn_4S_{16}$(Z=Mg, Mn, Zn, Cd, Sn, In, Bi, Sn) were grown by high temperature flux method. Single crystal X-ray diffraction combined with solid-state NMR spectroscopy were employed to confirm the structure models of $Ba_6(Cu_{2.9}Sn_{0.4})Sn_4S_{16}$. There is an interstitial atomic position partially occupied by a Sn atom in $Ba_6(Cu_{2.9}Sn_{0.4})Sn_4S_{16}$. The interstitial atomic position disappeared in $Ba_6(Cu_xZ_y)Sn_4S_{16}$(Z=Mg, Mn, Zn, Cd, Sn, In, Bi) with Cu jointly occupied with Z metals (Z= Mg, Mn, Zn, Cd, Sn, In, Bi) at the same position. The $Ba_6(Cu_xZ_y)Sn_4S_{16}$(Z=Mg, Mn, Zn, Cd, Sn, In, Bi) compounds are isostructural and belong to the $Ba_6Ag_4Sn_4S_{16}$ structure type. The ELF calculations and COHP calculations verified the ionic bonding characteristics of Ba-S interactions and Cu-S interactions. The Sn-S bonds were found as strong covalent bonds. The replacement of monovalent Cu atoms by various metals obviously shifts the optical properties of the $Ba_6(Cu_xZ_y)Sn_4S_{16}$(Z=Mg, Mn, Zn, Cd, Sn, In, Bi) compounds in a way that promotes a good balance between SHG and LDT. The DFT calculations confirmed that $[CuS_4]$ tetrahedra and $[SnS_4]$ tetrahedra are crucial for the structure stability and optical properties of $Ba_6(Cu_2Mg)Sn_4S_{16}$.

ASSOCIATED CONTENTS

Supporting Information

Crystallographic data, EDX results, room temperature powder X-ray diffraction data, UV-Vis data, Tauc plots, SHG measurements, DFT calculation, ^{119}Sn chemical shielding tensor parameters.

Acknowledgments

This research is supported by start-up funds from Wichita State University. Solid-state NMR experiments and data analysis (Y.C., A.J.R.) were supported by the U.S. Department of Energy (DOE), Office of Science, Basic Energy Sciences, Materials Science and Engineering Division. The Ames Laboratory is operated for the U.S. DOE by Iowa State University under Contract DE-AC02-07CH11358.

Corresponding author:

Bingbing Zhang zhangbb@hbu.edu.cn

Jian Wang jian.wang@wichita.edu

Notes

The authors declare no competing financial interest.

References

[1] Yu, M.; Okawachi, Y. ; Griffith, A. G.; Picqué, N.; Lipson, M.; Gaeta, A. L. Silicon-chip-based mid-infrared dual-comb spectroscopy. *Nat. Commun.* **2018**, *9*, 1869. https://doi.org/10.1038/s41467-018-04350-1

[2] Muraviev, A. V.; Smolski, V. O.; Loparo, Z. E.; Vodopyanov, K. L. Massively parallel sensing of trace molecules and their isotopologues with broadband subharmonic mid-infrared frequency combs. *Nature Photon.* **2018**, *12*, 209-214. https://doi.org/10.1038/s41566-018-0135-2

[3] J. S. Dam, P. Tidemand-Lichtenberg, C. Pedersen, Room-temperature mid-infrared single-photon spectral imaging. *Nature Photon.***2012**, *6*, 788-793. https://doi.org/10.1038/nphoton.2012.231

[4] Pestov, D.; Wang, X.; Ariunbold, G. O.; Murawski, R. K.; Sautenkov, V. A.; Dogariu, A.; Sokolov, A. V.; Scully, M. O. Single-Shot Detection of Bacterial Endospores via Coherent Raman Spectroscopy. *Proc. Natl. Acad. Sci. U. S. A.* **2008**, *105* (2), 422–427. DOI: 10.1073/pnas.0710427105

[5] Ok, K. M. Toward the Rational Design of Novel Noncentrosymmetric Materials: Factors Influencing the Framework Structures. *Acc. Chem. Res.* **2016**, *49* (12), 2774–2785. DOI: acs.accounts.6b00452

[6] Chung, I.; Kanatzidis, M. G. Metal Chalcogenides: A Rich Source of Nonlinear Optical Materials. *Chem. Mater.* **2014**, *26* (1), 849–869. DOI: 10.1021/cm401737s

[7] Kang, L.; Zhou, M.; Yao, J.; Lin, Z.; Wu, Y.; Chen, C. Metal Thiophosphates with Good Mid-Infrared Nonlinear Optical Performances: A First-Principles Prediction and Analysis. *J. Am. Chem. Soc.* **2015**, *137* (40), 13049–13059. DOI: 10.1021/jacs.5b07920

[8] Mei, D.; Cao, W.; Wang, N.; Jiang, X.; Zhao, J.; Wang, W.; Dang, J.; Zhang, S.; Wu, Y.; Rao, P.; Lin, Z. Breaking through the "3.0 EV Wall" of Energy Band Gap in Mid-Infrared Nonlinear Optical Rare Earth Chalcogenides by Charge-Transfer Engineering. *Mater. Horiz.* **2021**, *8* (8), 2330–2334. DOI: 10.1039/D1MH00562F

[9] Liang, F.; Kang, L.; Lin, Z.; Wu, Y. Mid-Infrared Nonlinear Optical Materials Based on Metal Chalcogenides: Structure–Property Relationship. *Cryst. Growth Des.* **2017**, *17* (4), 2254–2289. DOI: 10.1021/acs.cgd.7b00214

[10] Cui, X.; Xiao, J.; Wu, Y.; Du, P.; Si, R.; Yang, H.; Tian, H.; Li, J.; Zhang, W.-H.; Deng, D.; Bao, X. A Graphene Composite Material with Single Cobalt Active Sites: A Highly Efficient Counter Electrode for Dye-Sensitized Solar Cells. *Angew. Chem. Int. Ed Engl.* **2016**, *55* (23), 6708–6712. DOI: 10.1002/anie.201602097

[11] Wu, K.; Zhang, B.; Yang, Z.; Pan, S. New Compressed Chalcopyrite-like $Li_2BaM^{IV}Q_4$ (M^{IV} = Ge, Sn; Q = S, Se): Promising Infrared Nonlinear Optical Materials. *J. Am. Chem. Soc.* **2017**, *139* (42), 14885–14888. DOI: 10.1021/jacs.7b08966

[12] Chang, H.-Y.; Kim, S.-H.; Halasyamani, P. S.; Ok, K. M. Alignment of Lone Pairs in a New Polar Material: Synthesis, Characterization, and Functional Properties of $Li_2Ti(IO_3)_6$. *J. Am. Chem. Soc.* **2009**, *131* (7), 2426–2427. DOI: 10.1021/ja808469a

[13] Zhang, H.; Zhang, M.; Pan, S.; Dong, X.; Yang, Z.; Hou, X.; Wang, Z.; Chang, K. B.; Poeppelmeier, K. R. $Pb_{17}O_8Cl_{18}$: A Promising IR Nonlinear Optical Material with Large Laser Damage Threshold Synthesized in an Open System. *J. Am. Chem. Soc.* **2015**, *137* (26), 8360–8363. DOI: https://doi.org/10.1021/jacs.5b03986

[14] Ji, B.; Pandey, K.; Harmer, C. P.; Wang, F.; Wu, K.; Hu, J.; Wang, J. Centrosymmetric or Noncentrosymmetric? Transition Metals Talking in $K_2TGe_3S_8$(T = Co, Fe). *Inorg. Chem.* **2021**, *60* (14), 10603–10613. DOI: https://doi.org/10.1021/acs.inorgchem.1c01149

[15] Ji, B.; Guderjahn, E.; Wu, K.; Syed, T. H.; Wei, W.; Zhang, B.; Wang, J. Revisiting Thiophosphate $Pb_3P_2S_8$: A Multifunctional Material Combining a Nonlinear Optical Response and Photocurrent Response. *Phys. Chem. Chem. Phys.* **2021**, *23* (41), 23696–23702. DOI: https://doi.org/10.1039/D1CP03624F

[16] Abudurusuli, A.; Li, J.; Pan, S. A Review on the Recently Developed Promising Infrared Nonlinear Optical Materials. *Dalton Trans.* **2021**, *50* (9), 3155–3160. DOI: https://doi.org/10.1039/D1DT00054C

[17] Luo, M.; Liang, F.; Hao, X.; Lin, D.; Li, B.; Lin, Z.; Ye, N. Rational Design of the Nonlinear Optical Response in a Tin Iodate Fluoride $Sn(IO_3)_2F_2$. *Chem. Mater.* **2020**, *32* (6), 2615–2620. DOI: https://doi.org/10.1021/acs.chemmater.0c00196

[18] Yin, R.; Hu, C.; Lei, B.-H.; Pan, S.; Yang, Z. Lone Pair Effects on Ternary Infrared Nonlinear Optical Materials. *Phys. Chem. Chem. Phys.* **2019**, *21* (9), 5142–5147. DOI: https://doi.org/10.1039/C8CP07894G

[19] Gong, P.; Liu, X.; Kang, L.; Lin, Z. Inorganic Planar π-Conjugated Groups in Nonlinear Optical Crystals: Review and Outlook. *Inorg. Chem. Front.* **2020**, *7* (4), 839–852. DOI: https://doi.org/10.1039/C9QI01589B

[20] Kang, L.; Liang, F.; Jiang, X.; Lin, Z.; Chen, C. First-Principles Design and Simulations Promote the Development of Nonlinear Optical Crystals. *Acc. Chem. Res.* **2020**, *53* (1), 209–217. DOI: https://doi.org/10.1021/acs.accounts.9b00448

[21] Zhang, W.; Yu, H.; Wu, H.; Halasyamani, P. S. Phase-Matching in Nonlinear Optical Compounds: A Materials Perspective. *Chem. Mater.* **2017**, *29* (7), 2655–2668. DOI: https://doi.org/10.1021/acs.chemmater.7b00243

[22] Liu, Y.; Shen, Y.; Zhao, S.; Luo, J. Structure-Property Relationship in Nonlinear Optical Materials with π-Conjugated CO3 Triangles. *Coord. Chem. Rev.* **2020**, *407* (213152), 213152. DOI: https://doi.org/10.1016/j.ccr.2019.213152

[23] Chu, Y.; Li, G.; Su, X.; Wu, K.; Pan, S. A Review on the Development of Infrared Nonlinear Optical Materials with Triangular Anionic Groups. *J. Solid State Chem.* **2019**, *271*, 266–272. DOI: https://doi.org/10.1016/j.jssc.2018.10.051

[24] Lin, H.; Li, Y.-Y.; Li, M.-Y.; Ma, Z.; Wu, L.-M.; Wu, X.-T.; Zhu, Q.-L. Centric-to-Acentric Structure Transformation Induced by a Stereochemically Active Lone Pair: A New Insight for Design of IR Nonlinear Optical Materials. *J. Mater. Chem. C,* **2019**, *7* (16), 4638–4643. DOI: https://doi.org/10.1039/C9TC00647H

[25] Lin, H.; Wei, W.-B.; Chen, H.; Wu, X.-T.; Zhu, Q.-L. Rational Design of Infrared Nonlinear Optical Chalcogenides by Chemical Substitution. *Coord. Chem. Rev.* **2020**, *406* (213150), 213150. DOI: https://doi.org/10.1016/j.ccr.2019.213150

[26] Devi, M. S.; Vidyasagar, K. First Examples of Sulfides in the Quaternary A/Cd/Sn/S (A = Li, Na) Systems: Molten Flux Synthesis and Single Crystal X-Ray Structures of Li_2CdSnS_4, Na_2CdSnS_4 and $Na_6CdSn_4S_{12}$. ***J. Chem. Soc., Dalton Trans.,*** **2002**, 2092–2096. DOI: https://doi.org/10.1039/B110254K

[27] Zhang, J.-H.; Clark, D. J.; Brant, J. A.; Rosmus, K. A.; Grima, P.; Lekse, J. W.; Jang, J. I.; Aitken, J. A. α-Li_2ZnGeS_4: A Wide-Bandgap Diamond-like Semiconductor with Excellent

Balance between Laser-Induced Damage Threshold and Second Harmonic Generation Response. *Chem. Mater.* **2020**, *32* (20), 8947–8955. DOI: https://doi.org/10.1021/acs.chemmater.0c02929

[28] Devlin, K. P.; Glaid, A. J.; Brant, J. A.; Zhang, J.-H.; Srnec, M. N.; Clark, D. J.; Soo Kim, Y.; Jang, J. I.; Daley, K. R.; Moreau, M. A.; Madura, J. D.; Aitken, J. A. Polymorphism and Second Harmonic Generation in a Novel Diamond-like Semiconductor: Li_2MnSnS_4. *J. Solid State Chem.* **2015**, *231*, 256–266. DOI: https://doi.org/10.1016/j.jssc.2015.08.011

[29] Chen, J.; Chen, H.; Xu, F.; Cao, L.; Jiang, X.; Yang, S.; Sun, Y.; Zhao, X.; Lin, C.; Ye, N. $Mg_2In_3Si_2P_7$: A Quaternary Diamond-like Phosphide Infrared Nonlinear Optical Material Derived from ZnGeP2. *J. Am. Chem. Soc.* **2021**, *143* (27), 10309–10316. DOI: https://doi.org/10.1021/jacs.1c03930

[30] Liu, X.; Kang, L.; Gong, P.; Lin, Z. $LiZn(OH)CO_3$: A Deep-Ultraviolet Nonlinear Optical Hydroxycarbonate Designed from a Diamond-like Structure. *Angew. Chem. Int. Ed.* **2021**, *60* , 13574–13578. DOI: https://doi.org/10.1002/anie.202101308

[31] Rosmus, K. A.; Brant, J. A.; Wisneski, S. D.; Clark, D. J.; Kim, Y. S.; Jang, J. I.; Brunetta, C. D.; Zhang, J.-H.; Srnec, M. N.; Aitken, J. A. Optical Nonlinearity in Cu_2CdSnS_4 and α/β-Cu_2ZnSiS_4: Diamond-like Semiconductors with High Laser-Damage Thresholds. *Inorg. Chem.* **2014**, *53* (15), 7809–7811. DOI: https://doi.org/10.1021/ic501310d

[32] Li, M.-Y.; Ma, Z.; Li, B.; Wu, X.-T.; Lin, H.; Zhu, Q.-L. $HgCuPS_4$: An Exceptional Infrared Nonlinear Optical Material with Defect Diamond-like Structure. *Chem. Mater.* **2020**, *32* (10), 4331–4339. DOI: https://doi.org/10.1021/acs.chemmater.0c01258

[33] Guo, Y.; Liang, F.; Li, Z.; Xing, W.; Lin, Z.; Yao, J.; Wu, Y. $Li_4HgSn_2Se_7$: The First Second-Order Nonlinear Optical-Active Selenide in the I_4–II–IV_2–VI_7 Diamond-like Family. *Cryst. Growth Des.* **2019**, *19* (10), 5494–5497. DOI: https://doi.org/10.1021/acs.cgd.9b01074

[34] Yang, Y.; Chu, Y.; Zhang, B.; Wu, K.; Pan, S. Unique Unilateral-Chelated Mode-Induced d–P−π Interaction Enhances Second-Harmonic Generation Response in New Ln_3LiMS_7

Family. *Chem. Mater.* **2021**, *33* (11), 4225–4230. DOI: https://doi.org/10.1021/acs.chemmater.1c01133

[35] Shi, Y.-F.; Chen, Y.-K.; Chen, M.-C.; Wu, L.-M.; Lin, H.; Zhou, L.-J.; Chen, L. Strongest Second Harmonic Generation in the Polar R_3MTQ_7 Family: Atomic Distribution Induced Nonlinear Optical Cooperation. *Chem. Mater.* **2015**, *27* (5), 1876–1884. DOI: https://doi.org/10.1021/acs.chemmater.5b00177

[36] He, J.; Wang, Z.; Zhang, X.; Cheng, Y.; Gong, Y.; Lai, X.; Zheng, C.; Lin, J.; Huang, F. Synthesis, Structure, Magnetic and Photoelectric Properties of $Ln_3M_{0.5}M'Se_7$ (Ln = La, Ce, Sm; M = Fe, Mn; M′ = Si, Ge) and $La_3MnGaSe_7$. *RSC Adv.* **2015**, *5* (65), 52629–52635. DOI: https://doi.org/10.1039/C5RA05629B

[37] Guo, S.-P.; Guo, G.-C.; Wang, M.-S.; Zou, J.-P.; Xu, G.; Wang, G.-J.; Long, X.-F.; Huang, J.-S. A Series of New Infrared NLO Semiconductors, $ZnY_6Si_2S_{14}$, $Al_xDy_3(Si_yAl_{1-y})S_7$, and $Al_{0.33}Sm_3SiS_7$. *Inorg. Chem.* **2009**, *48* (15), 7059–7065. DOI: https://doi.org/10.1021/ic802443n

[38] Poduska, K. M.; Cario, L.; DiSalvo, F. J.; Min, K.; Halasyamani, P. S. Structural Studies of a Cubic, High-Temperature (α) Polymorph of Pb_2GeS_4 and the Isostructural $Pb_{2-x}Sn_xGeS_{4-y}Se_y$ Solid Solution. *J. Alloys Compd.* **2002**, *335* (1–2), 105–110. DOI: https://doi.org/10.1016/S0925-8388(01)01836-9

[39] Choudhury, A.; Dorhout, P. K. Alkali-Metal Thiogermanates: Sodium Channels and Variations on the La_3CuSiS_7 Structure Type. *Inorg. Chem.* **2015**, *54* (3), 1055–1065. DOI: https://doi.org/10.1021/ic502418s

[40] Rudyk, B. W.; Stoyko, S. S.; Mar, A. Rare-Earth Transition-Metal Indium Sulphides RE_3FeInS_7 (RE=La–Pr), RE_3CoInS_7 (RE=La, Ce), and La_3NiInS_7. *J. Solid State Chem.* **2013**, *208*, 78–85. DOI: https://doi.org/10.1016/j.jssc.2013.09.035

[41] Yin, W.; Shi, Y.; Kang, B.; Deng, J.; Yao, J.; Wu, Y. Rare-Earth Transition-Metal Chalcogenides Ln_3MGaS_7 (Ln=Nd, Sm, Dy, Er; M=co, Ni) and Ln_3MGaSe_7 (Ln=Nd, Sm, Gd, Dy, M=co; Ln=Nd, Gd, Dy, M=Ni). *J. Solid State Chem.* **2014**, *213*, 87–92. DOI: https://doi.org/10.1016/j.jssc.2014.01.033

[42] Duan, R.; Lin, H.; Wang, Y.; Zhou, Y.; Wu, L. Non-Centrosymmetric Sulfides $A_2Ba_6MnSn_4S_{16}$ (A = Li, Ag): Syntheses, Structures and Properties. *Dalton Trans.* **2020**, *49* (18), 5914–5920. DOI: https://doi.org/10.1039/D0DT00894J

[43] Yang, Y.; Song, M.; Zhang, J.; Gao, L.; Wu, X.; Wu, K. Coordinated Regulation on Critical Physiochemical Performances Activated from Mixed Tetrahedral Anionic Ligands in New Series of $Sr_6A_4M_4S_{16}$ (A = Ag, Cu; M = Ge, Sn) Nonlinear Optical Materials. *Dalton Trans.* **2020**, *49* (11), 3388–3392. DOI: https://doi.org/10.1039/D0DT00432D

[44] Cao, W.; Mei, D.; Yang, Y.; Wu, Y.; Zhang, L.; Wu, Y.; He, X.; Lin, Z.; Huang, F. From $CuFeS_2$ to $Ba_6Cu_2FeGe_4S_{16}$: Rational Band Gap Engineering Achieves Large Second-Harmonic-Generation Together with High Laser Damage Threshold. *Chem. Commun. (Camb.)* **2019**, *55* (96), 14510–14513. DOI: https://doi.org/10.1039/C9CC07288H

[45] Zhang, L.; Mei, D.; Wu, Y.; Shen, C.; Hu, W.; Zhang, L.; Li, J.; Wu, Y.; He, X. Syntheses, Structures, Optical Properties, and Electronic Structures of $Ba_6Cu_2GSn_4S_{16}$ (G = Fe, Ni) and $Sr_6D_2FeSn_4S_{16}$ (D = Cu, Ag). *J. Solid State Chem.* **2019**, *272*, 69–77. DOI: https://doi.org/10.1016/j.jssc.2019.01.024

[46] Duan, R.-H.; Liu, P.-F.; Lin, H.; Zheng, Y. J.; Yu, J.-S.; Wu, X.-T.; Huang-Fu, S.-X.; Chen, L. $Ba_6Li_2CdSn_4S_{16}$: Lithium Substitution Simultaneously Enhances Band Gap and SHG Intensity. *J. Mater. Chem. C,***2017**, *5* (28), 7067–7074. DOI: https://doi.org/10.1039/C7TC01811H

[47] Duan, R.-H.; Li, R.-A.; Liu, P.-F.; Lin, H.; Wang, Y.; Wu, L.-M. Modifying Disordered Sites with Rational Cations to Regulate Band-Gaps and Second Harmonic Generation Responses Markedly: $Ba_6Li_2ZnSn_4S16$ vs $Ba_6Ag_2ZnSn_4S_{16}$ vs $Ba_6Li_{2.67}Sn_{4.33}S_{16}$. *Cryst. Growth Des.* **2018**, *18* (9), 5609–5616. DOI: https://doi.org/10.1021/acs.cgd.8b00927

[48] Abudurusuli, A.; Wu, K.; Pan, S. Four New Quaternary Chalcogenides $A_2Ba_7Sn_4Q_{16}$ (A = Li, Na; Q = S, Se): Syntheses, Crystal Structures Determination, Nonlinear Optical Performances Investigation. *New J Chem* **2018**, *42* (5), 3350–3355. DOI: https://doi.org/10.1039/C7NJ04288D

[49] Lai, W.-H.; Haynes, A. S.; Frazer, L.; Chang, Y.-M.; Liu, T.-K.; Lin, J.-F.; Liang, I.-C.; Sheu, H.-S.; Ketterson, J. B.; Kanatzidis, M. G.; Hsu, K.-F. Second Harmonic Generation Response Optimized at Various Optical Wavelength Ranges through a Series of Cubic Chalcogenides $Ba_6Ag_{2.67+4\delta}Sn_{4.33-\delta}S_{16-X}Se_x$. *Chem. Mater.* **2015**, *27* (4), 1316–1326. DOI: https://doi.org/10.1021/cm504348z

[50] Lian, Y.-K.; Li, R.-A.; Liu, X.; Wu, L.-M.; Chen, L. $Sr_6(Li_2Cd)A_4S_{16}$ (A = Ge, Sn): How to Go beyond the Band Gap Limitation via Site-Specific Modification. *Cryst. Growth Des.* **2020**, *20* (12), 8084–8089. DOI: https://doi.org/10.1021/acs.cgd.0c01368

[51] Cicirello, G.; Wu, K.; Wang, J. Synthesis, Crystal Structure, Linear and Nonlinear Optical Properties of Quaternary Sulfides $Ba_6(Cu_2X)Ge_4S_{16}$ (X=Mg, Mn, Cd). *J. Solid State Chem.* **2021**, *300* (122226), 122226. DOI: https://doi.org/10.1016/j.jssc.2021.122226

[52] *Bruker APEX2*; Bruker AXS Inc.: Madison, WI, 2005

[53] Sheldrick, G. M. A Short History of SHELX. *Acta Crystallogr., Sect. A: Found. Crystallogr.* **2008**, *64*, 112– 122. DOI: 10.1107/S0108767307043930

[54] Parthé, E.; Gelato, L. M. The Standardization of Inorganic Crystal-Structure Data. *Acta Crystallogr., Sect. A: Found. Crystallogr.* **1984**, *40*, 169– 183. DOI: 10.1107/S0108767384000416

[55] Gelato, L. M.; Parthé, E. STRUCTURE TIDY– a Computer Program to Standardize Crystal Structure Data. *J. Appl. Crystallogr.* **1987**, *20*, 139– 143. DOI: 10.1107/S0021889887086965

[56] Kurtz, S. K.; Perry, T. T. A Powder Technique for the Evaluation of Nonlinear Optical Materials. *J. Appl. Phys.* **1968**, *39*, 3798. DOI: 10.1063/1.1656857

[57] Kresse, G.; Hafner, J. Ab Initio Molecular Dynamics for Liquid Metals. *Phys. Rev. B: Condens. Matter Mater. Phys.* **1993**, *47*, 558– 561. DOI: 10.1103/PhysRevB.47.558

[58] Kresse, G.; Hafner, J. Ab Initio Molecular-Dynamics Simulation of the Liquid-Metal-Amorphous-Semiconductor Transition in Germanium. *Phys. Rev. B: Condens. Matter Mater. Phys.* **1994**, *49*, 14251– 14269. DOI: 10.1103/PhysRevB.49.14251

[59] Kresse, G.; Furthmüller, J. Efficiency of Ab-Initio Total Energy Calculations for Metals and Semiconductors Using a Plane-Wave Basis Set. *Comput. Mater. Sci.* **1996**, *6*, 15– 50. DOI: 10.1016/0927-0256(96)00008-0

[60] Kresse, G.; Furthmüller, J. Efficient Iterative Schemes for Ab Initio Total-Energy Calculations Using a Plane-Wave Basis Set. *Phys. Rev. B: Condens. Matter Mater. Phys.* **1996**, *54*, 11169–11186. DOI: 10.1103/PhysRevB.54.11169

[61] Kresse, G.; Joubert, D. From Ultrasoft Pseudopotentials to the Projector Augmented-Wave Method. *Phys. Rev. B: Condens. Matter Mater. Phys.* **1999**, *59*, 1758– 1775. DOI: 10.1103/PhysRevB.59.1758

[62] Perdew, J. P.; Burke, K.; Ernzerhof, M. Generalized Gradient Approximation Made Simple. *Phys. Rev. Lett.* **1996**, *77*, 3865– 3868. DOI: 10.1103/PhysRevLett.77.3865

[63] Monkhorst, H. J.; Pack, J. D. Special Points for Brillouin-Zone Integrations. *Phys. Rev. B: Condens. Matter Mater. Phys.* **1976**, *13*, 5188– 5192. DOI: 10.1103/PhysRevB.13.5188

[64] O. Jepsen, A. Burkhardt and O. K Andersen, *The Program TB-LMTO-ASA, Version4.7*, Max-Planck-Institut für Festkörperforschung, Stuttgart, Germany, 1999.

[65] U. von Barth and L. Hedin, A local exchange-correlation potential for the spin polarized case. *J. phys.*, 1972, **5**, 1629–1642.

[66] Pfrommer, B. G.; Côté, M.; Louie, S. G.; Cohen, M. L. Relaxation of Crystals with the Quasi-Newton Method. *J. Comput. Phys.* **1997**, *131* (1), 233–240. DOI: https://doi.org/10.1006/jcph.1996.5612

[67] Perdew, J. P.; Burke, K.; Ernzerhof, M. Generalized Gradient Approximation Made Simple. *Phys. Rev. Lett.* **1997**, *78* (7), 1396–1396. DOI: https://doi.org/10.1103/PhysRevLett.78.1396

[68] Rappe, A. M.; Rabe, K. M.; Kaxiras, E.; Joannopoulos, J. D. Optimized Pseudopotentials. *Phys. Rev. B Condens. Matter* **1990**, *41* (2), 1227–1230. DOI: https://doi.org/10.1103/PhysRevB.41.1227

[69] Harris, R. K.; Becker, E. D.; Cabral de Menezes, S. M.; Goodfellow, R.; Granger, P., NMR nomenclature. Nuclear spin properties and conventions for chemical shifts (IUPAC Recommendations 2001). *Pure Appl. Chem.* **2001,** *73* (11), 1795-1818. DOI: https://doi.org/10.1351/pac200173111795

[70] Fung, B. M.; Khitrin, A. K.; Ermolaev, K., An Improved Broadband Decoupling Sequence for Liquid Crystals and Solids. *J. Magn. Reson.* **2000,** *142* (1), 97-101. DOI: https://doi.org/10.1006/jmre.1999.1896

[71] Clark, S. J.; Segall, M. D.; Pickard, C. J.; Hasnip, P. J.; Probert, M. I. J.; Refson, K.; Payne, M. C., First principles methods using CASTEP. *Z. Kristallogr. Cryst. Mater.* **2005,** *220* (5-6), 567-570. DOI: https://doi.org/10.1524/zkri.220.5.567.65075

[72] Yates, J. R.; Pickard, C. J.; Mauri, F., Calculation of NMR chemical shifts for extended systems using ultrasoft pseudopotentials. *Phys. Rev. B* **2007,** *76* (2), 024401. DOI: https://doi.org/10.1103/PhysRevB.76.024401

[73] Pickard, C. J.; Mauri, F., All-electron magnetic response with pseudopotentials: NMR chemical shifts. *Phys. Rev. B* **2001,** *63* (24), 245101. DOI: https://doi.org/10.1103/PhysRevB.63.245101

[74] Chen, H.; Liu, P.-F.; Li, B.-X.; Lin, H.; Wu, L.-M.; Wu, X.-T. Experimental and Theoretical Studies on the NLO Properties of Two Quaternary Non-Centrosymmetric Chalcogenides: $BaAg_2GeS_4$and $BaAg_2SnS_4$. Dalton Trans. 2018, 47 (2), 429–437. DOI: https://doi.org/10.1039/C7DT04178K

[75] Chu, Y.; Wu, K.; Su, X.; Han, J.; Yang, Z.; Pan, S. Intriguing Structural Transition Inducing Variable Birefringences in ABa_2MS_4Cl (A = Rb, Cs; M = Ge, Sn). *Inorg. Chem.* **2018**, *57* (18), 11310–11313. DOI: https://doi.org/10.1021/acs.inorgchem.8b01788

[76] Duan, R.-H.; Liu, P.-F.; Lin, H.; Huangfu, S.-X.; Wu, L.-M. Syntheses and Characterization of Three New Sulfides with Large Band Gaps: Acentric $Ba_4Ga_4SnS_{12}$, Centric $Ba_{12}Sn_4S_{23}$ and $Ba_7Sn_3S_{13}$. *Dalton Trans.* **2017**, *46* (43), 14771–14778. DOI: https://doi.org/10.1039/C7DT03267F

[77] Luo, Z.-Z.; Lin, C.-S.; Zhang, W.-L.; Zhang, H.; He, Z.-Z.; Cheng, W.-D. $Ba_8Sn_4S_{15}$: A Strong Second Harmonic Generation Sulfide with Zero-Dimensional Crystal Structure. *Chem. Mater.* **2014**, *26* (2), 1093–1099. DOI: https://doi.org/10.1021/cm403369m

[78] Ye, Z.; Peng, W.; Wang, F.; Balodhi, A.; Basnet, R.; Hu, J.; Zevalkink, A.; Wang, J. Quasi-Layered Crystal Structure Coupled with Point Defects Leading to Ultralow Lattice Thermal Conductivity in n-Type $Cu_{2.83}Bi_{10}Se_{16}$. *ACS Appl. Energy Mater.* **2021**, *4* (10), 11325–11335. DOI: https://doi.org/10.1021/acsaem.1c02154

[79] Li, S.-F.; Jiang, X.-M.; Fan, Y.-H.; Liu, B.-W.; Zeng, H.-Y.; Guo, G.-C. New strategy for designing promising mid-infrared nonlinear optical materials: narrowing the band gap for large nonlinear optical efficiencies and reducing the thermal effect for a high laser-induced damage threshold. *Chem. Sci.*, **2018**, *9,* 5700–5708. DOI: https://doi.org/10.1039/C8SC01210E

[80] Chen, H.; Wei, W.-B.; Lin, H.; Wu, X.-T. Transition-metal-based chalcogenides: A rich source of infrared nonlinear optical materials. *Coord. Chem. Rev.*, **2021**, *448,* 214154. DOI: https://doi.org/10.1016/j.ccr.2021.214154

[81] Chen, M.-M.; Zhou, S.-H.; Wei, W.-B. ;Wu, X.-T.; Lin, H. ; Zhu, Q.-L. Phase Matchability Transformation in the Infrared Nonlinear Optical Materials with Diamond-Like Frameworks. *Adv. Opt. Mater.*, **2021**, 2102123. https://doi.org/10.1002/adom.202102123

For Table of Contents Only

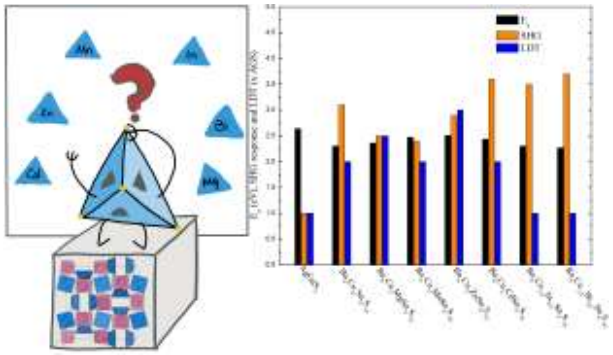

Seven acentric sulfides $Ba_6(Cu_xZ_y)Sn_4S_{16}$(Z=Mg, Mn, Zn, Cd, In, Bi) exhibit excellent chemical flexibility due to the replacement of monovalent Cu atoms by various metals, which results in good nonlinear optical properties.